El-Rayes *et al.*
Environmental Systems Research (2023) 12:21
https://doi.org/10.1186/s40068-023-00306-7

Environmental Systems Research

RESEARCH

Open Access

Geo-hazards assessment of the new-found industrial communities: an example from the 10th of Ramadan Industrial Region, Egypt

Ahmed E. El-Rayes[1*], Mohamed O. Arnous[1], David R. Green[2] and Norhan F. Gouda[1]

Abstract

The impacts of Geo-hazard events are main obstacles to the use of land in numerous arid and semi-arid provinces of the World. Furthermore, the various activities of industrial communities, such as Egypt's 10th Ramadan Industrial Region (10th RIR), are the most dangerous examples of waste's impact on soil, surface water, and groundwater. The current study uses image processing and GIS tools to identify, delineate, monitor, and assess some of the environmental hazards caused by both human and natural activities in the 10th RIR. The findings revealed that there are rapid changes in land cover, which could be attributed to both anthropogenic and natural activities. Furthermore, the results revealed that waterlogging, salt-affected soils, water pollution, and flash floods were the most serious environmental threats to the 10th RIR. The obtained geo-hazard map showed that the 10th RIR has high flash flood hazards zones that are geospatially distributed in the southern parts of the Wadi Gafra basin and the western parts of 10th of Ramadan City. Furthermore, salinized soil zones are viewed as geospatially restricted zone in the eastern portion of 10th of Ramadan City and/or near the oxidation ponds. Additionally, vast areas of highly contaminated groundwater exist beneath industrial, urban, and oxidation pond zones. The current work provides decision-makers with numerous mitigation measures and recommendations required to minimize the impacts of geo-environmental hazards endangering the 10th RIR.

Keywords Flash floods, Waterlogging, Sustainable development, Groundwater pollution, GIS

Introduction

Today economic progress produces a large-scale construction, weighty development projects, and development of new land which revitalized undesired consequences and led to new ones not identified before in the environmental status. These developments have become keystones of the mainly new environmental impact problems of the protection and sustainable use of natural resources. Consequently, difficulties encountered have been due to new conceptualizations of the environment. To develop an applicable sustainable plan for a desert area development, a precise geo-environmental assessment of the considered area would be an important step.

Geo-environmental assessment is based on two things; these are the resource inventory and the hazards mitigation measures (Arnous 2004, Arnous and Green 2011, Arnous et al. 2011). Egypt has undergone several economic and social periods. Egypt's economic crisis is the export–import unbalance, or in other words an increase

*Correspondence:
Ahmed E. El-Rayes
ahmed_elrais@science.suez.edu.eg
[1] Geology Department, Faculty of Science, Suez Canal University, Ismailia 41522, Egypt
[2] Department of Geography and Environment, School of Geosciences, University of Aberdeen, Aberdeen AB24 3FX, UK

in consumption with a decrease in production. The social problem can be summarized by the high rate of population growth, the shortage of job opportunities and the absence of applicable development planning for the vast desert areas surrounding the Nile Valley and Delta (Arnous 2004).

The natural and man-made geo-hazard assessments are required for the accurate planning and management of future environmental hazards impacts (Arnous et al. 2011, Arnous and Green 2011, El-Rayes et al. 2015). Every year, geo-hazards destroy lives and hard-won progress in communities, and may require a long time to recover from the consequences of geo-hazards. However, good policy and planning can prevent losses in the first place (Sandler and Schwab 2022).

Geo-environmental hazards such as waterlogging, flash flooding, soil salinization, water pollution, seismic activity, rock fall, sand dune encroachment, and landslides constitute the main natural threats. These threats are impacted the socio-economic and environmental settings such as loss of life, damage of the infrastructure, buildings, industrial projects and private businesses inhabiting the affected zones (El-Rayes et al. 2015; Elbeih et al. 2021; Moubarak et al. 2021; Omran et al. 2021). Because of this, hazard management decisions must to be taken based on availability of scientific databases (Arnous 2011). Various hazards assessment integration models have been developed to assess the probability of each hazard level (Lin et al. 2020, 2022; Lyu et al. 2019; Chen et al. 2022; Yan et al. 2022). Today, the land-use/land-cover changes are quick, active and affect the socio-economic situations, specifically nearby the main urban areas, industrial communities, agricultural and tourist regions (Arnous et al. 2017).

The 10th of Ramadan Industrial Region (10th RIR) is located near to the Nile delta and its valley. It is rich in natural resources and surrounded by Suez, Ismailia, Greater Cairo, and Sharkiya Governorates. In 1984 the Egyptian Government initiates the first stage of the urban invasion of the desert by establishing of the 10th RIR as a new industrial center. The development of this area can help to solve both the economic and social problems of Egypt as a new industrial community (Arnous 2004). The Greater Cairo zone has had the chief share of urban invasion into the Egyptian desert lands. The population density of the target area expected to be increased to nearly the double of its current inhabitance by 2050 (Sims 2010). Greater Cairo zone offers the premier chance of a growth in employment opportunities in Egypt due to the creation of new industrial units and farms nearby the target area. Recently, the northeastern sector of Cairo, in which numerous new-found industrial units were established, like the 10th RIR, is threatened by obvious environmental deteriorations. These environmental threats were mainly resulted by the human activities impacting the natural resources. Water resources are essential to any sustainable industrial development. During the last three decades, the 10th RIR experiences a rapid development in various types of activities like agricultural, industrial, urban, and developing projects especially nearby the water sources. Then, the wastewater drainage of the 10th RIR activities impacted the shallow aquifer and surface soil (Hefny et al. 1980, Gad 1995, Embaby and El Haddad 2007, Abu El Ela 2008, Elnemr et al. 2015, Hussien et al. 2017, Hussein et al. 2019, Gouda 2019). Therefore, land use/ land cover mapping (LULC) is an essential factor to understand the impacts of the human and natural activities on the environment. Subsequently, it is crucial for monitoring and detecting the environmental alterations to conserve the sustainable environment. Numerous studies utilize remote sensing and GIS tools in conjunction with fieldwork and hydrogeological examinations to identify, assess, and map the geo-environmental hazards for sustainable development planning all over the world (Mejfa-Navarro et al. 1994, Bell and Culshaw 1998, Ramkumar 2009, Arnous and El-Rayes 2013, Ghodeif et al. 2013, Arnous and Green 2015, Cigna et al. 2015, Arnous et al. 2015, Hadian et al. 2016, El-Rayes et al. 2017, Sun et al. 2017, Dobrescu et al. 2017, Lyu et al. 2018, Arnous and Omar 2018).

The 10th RIR has experienced some challenging changes in the hydrogeological and environmental conditions as a result of the expanding population and industrial projects (Embaby and El Haddad 2007, Abu El Ela 2008, El-Sayed et al. 2012, Attwa et al. 2013, Elnemr et al. 2015, Hussien et al. 2017, Gouda 2019, Hussein et al. 2019, Elbeih 2021). Land degradation and various geo-hazards are two ways that the challenging changes are expressed. Waterlogging, industrial wastewater reservoirs (oxidation ponds), soil salinization, flash floods, and various types of pollution are the most prevalent geo-hazards that endanger the natural resources of the 10th RIR (Additional file 1: Fig. S1). The degradation of natural resources, such as soil, water, and air, is thought to be one of the most dangerous effects of industrial activity. These resources are particularly vulnerable to contamination by heavy metals produced by the disposal of industrial waste (Gad 1995, Arnous and El-Rayes 2013, Chintalapudi et al. 2017, Hussein et al. 2019).

The current study aims to identify, delineate, monitor, and assess the most prominent geo-hazards produced by human and natural activities, including flash floods, groundwater pollution, and land degradation in the 10th RIR. This study is unique from earlier studies in this particular field as it is the first to perform an extensive evaluation of all potential hazards that arise from human

or natural activities, influencing the 10th RIR. The morphometric analysis approach, the hydrogeochemical data, and the digital image processing of multi-temporal satellite data are used in the typical standard sequence to achieve the main objective of the work. It also entails creating various LULC and thematic maps, using GIS modeling to create geo-hazard maps by integrating thematic maps and other ancillary geological data. Finally, mitigation strategies would be developed in the 10th RIR to reduce or prevent the negative impacts of common geo-hazards.

The study area

The 10th RIR is situated along the Cairo—Ismailia Desert Highway, 46 km from Cairo between longitudes 31°36′ and 32°00′E and latitudes 30°00′ and 30°24′N and covers an area of about 2850 km^2 (Fig. 1B). It is bounded to the north by the Ismailia fresh water canal, to the south by the Cairo—Suez desert road to the east by Gabal (G.) Umm Raqam and G. Hafa, to the west by G. Umm Qamer and G. El-Hamza (Fig. 1C). The study area is crossed by the Cairo—Ismailia high way and is accessible by a four-wheel drive car through well-maintained desert tracks and asphalt roads. It is also accessible by paved roads such as the Belbeis-10th Ramadan and Cairo-Suez desert roads as well as several tracks. Generally, the majority of the study area forming a semi-flat landscape. Numerous wadis (valleys) of various trends dissect the study area such as, Wadi (W.) Gafra, W. El-Hamza and W. Sakran (Fig. 1C). The 10th RIR is bounded by a chain of ridges and scarps originating in the Oligocene, Miocene, Pliocene age and Holocene Age (El-Fayoumy 1968, El-Shazly et al. 1975, Arnous 2004). The ground elevation of the 10th RIR increases from 12 m + msl in the northern areas, to about 80 m + msl in the southern areas with common slopes in the direction of the northern and northeastern.

The weather in the city of 10th of Ramadan is referred to as a desert climate, with hot, dry summers and mild, rainy winters. The difference in precipitation between the wettest and driest months is 5 mm. June is the driest month with 0 mm of precipitation. In January, the precipitation reaches its peak, with an average of 5 mm.

The annual precipitation total is about 20 mm. The annual average temperature is 21.2 °C. August is the warmest month, with an average temperature of 28.3 °C. January is the coldest month of the year, with an average temperature of 12.9 °C. The highest relative humidity index is 55.17% in December. May has the lowest relative humidity (39.53%) of any month (Climate-Data.org. 2013).

Evaporation is highest from April to July (14 mm/day at Cairo metrological station) and lowest in December (4.3 mm/day at Belbies metrological station). The evaporation pattern is determined by the relative humidity values in the study area. The high evaporation rate and low precipitation intensity have a significant impact on groundwater recharge and water quality at the 10th RIR.

Geology of the 10th RIR

The 10th RIR is sited at the southeastern portion of East Nile Delta, Egypt. It's mostly occupied by sedimentary rocks of Tertiary and Quaternary period (Said 1990). The lithological map shows that Pleistocene sediments cover almost 85% of the map, primarily in the northern and eastern sectors (Fig. 2). They are primarily composed of aeolian sands and fluvial deposits intercalated with gravel and clay, and they superimpose the Tertiary deposits unconformably. The Pliocene sediments, composed of fossiliferous dark clay, have limited exposures along the study area's southern boundary (Fig. 2). They are also found in the subsurface units of the surrounding area (Khalaf and Gad 2015). The Miocene rocks cover about 15% of the map and are mostly composed of sands and clays from shallow marine sources (Said 1981). The Oligocene sediments are well cropped out at G. El-Hamza and G. Um El-Qamar, where they unconformably superimposed the Upper Eocene deposits. The wadi-filling sediments, which are mostly sands, flints, and quartzite cobbles, occupy the bottoms of the main streams in the mapped area.

Hydrogeology of the 10th RIR

Groundwater and aquifers distributions of the 10th RIR

The aquifers of the 10th RIR are hydrogeologically derived from the Nile aquifer, which forms a complex aquifer system. The Nile aquifer is made up of a leaky Pleistocene formation overlain by a leaky Holocene aquitard unit and underlain by an impervious Miocene aquiclude unit (Fig. 3). The bottom boundary of the deltaic sediments is a thick clay stratum that functions as an aquiclude border, defining the aquifer geometry (Sherif 1999).

The main sources of aquifer recharge are Nile River seepage water, canals, drains, and returned-flow irrigation water. While some of the aquifer's storage is discharged into the Ismailia canal along a portion of its course (Geriesh et al. 2008), it may also be discharged as effluent to the drainage system to the northern part of the 10th RIR. The aquifer base slopes generally northeastward, controlled by the dominant faulting system in the study area (El-Dairy 1980). In general, groundwater flows from south to north and northwest (Fig. 4); however, groundwater flow with local discharge sites may be redirected to the east via the Suez Canal (Ismael 2007; Elewa et al. 2013).

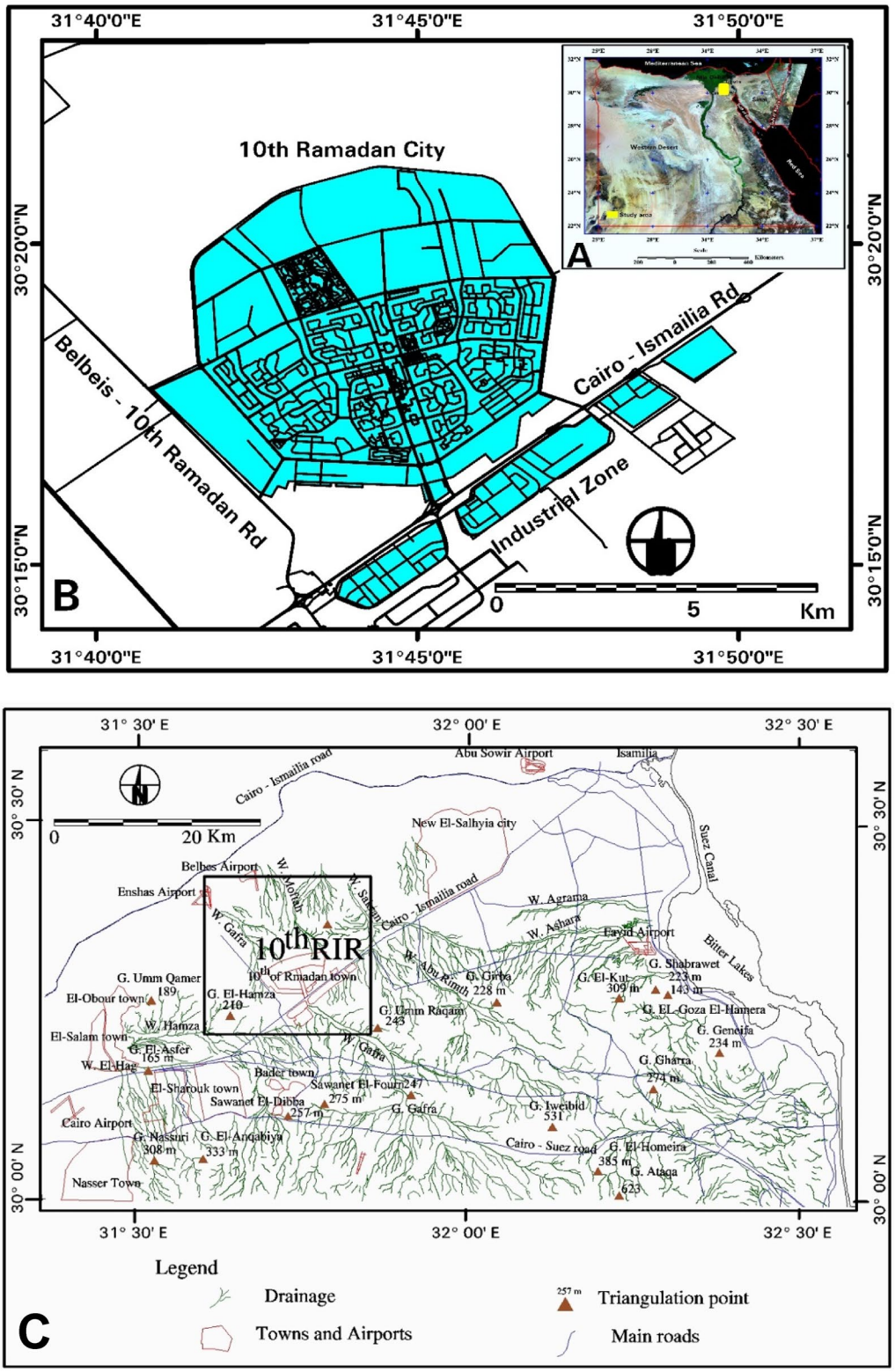

Fig. 1 Key (**A**) and location (**B**) maps of the 10th RIR illustrating primary roadways, and the physiographic map of the 10th RIR (**C**) displaying the major topographic summits and wadis (Arnous 2004)

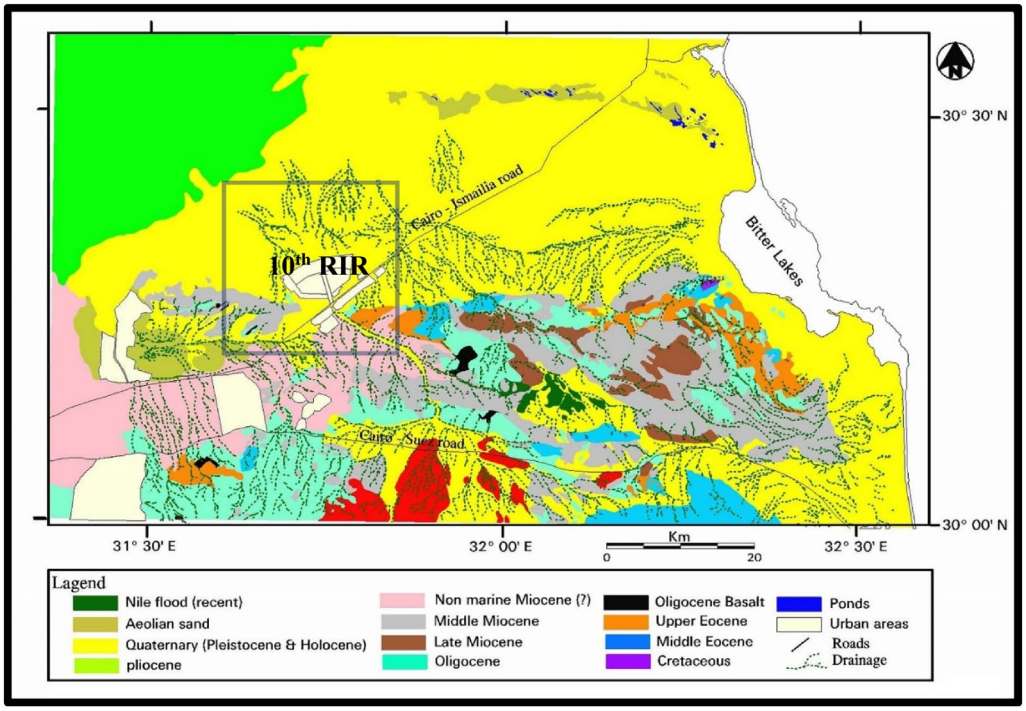

Fig. 2 Surface lithological map of the 10th RIR and its surrounds, displaying the areal distribution of rock units encountered (Arnous 2004)

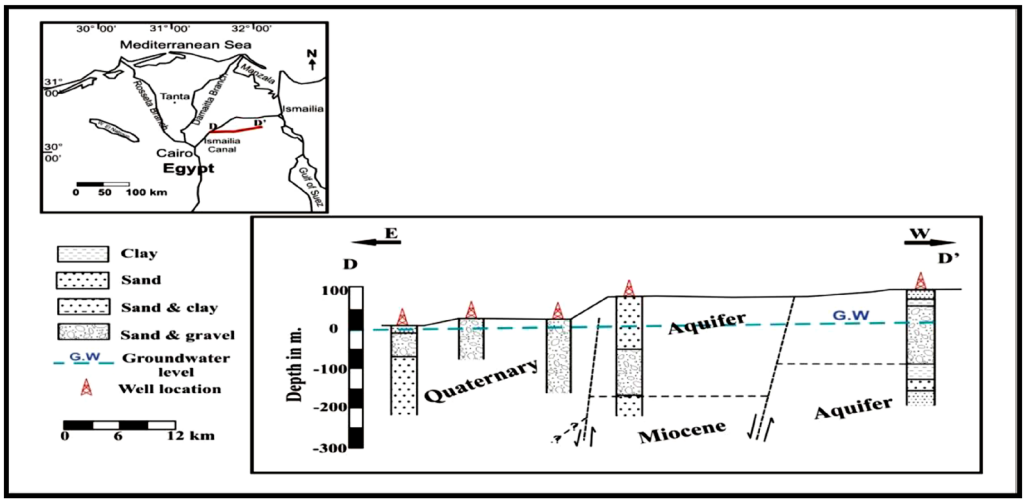

Fig. 3 An E-W hydrogeological cross-section of the 10th RIR describing the lateral variations of Quaternary and Miocene aquifers (Ibrahim et al. 2005)

Wells in the Pleistocene aquifer unit in the 10th RIR region were used for obtaining groundwater samples. Water level measurements have been made in only a few of the wells in the 10th RIR, despite the fact that the bulk of them have been totally sealed and have pumps attached to them, making it challenging to measure their water levels (Table 1).

Surface water of the 10th RIR

Surface water bodies spread, sparsely as waterlogging and extensively as oxidation ponds, along the ground surface of the10th RIR. The waterlogged part is the water held in the ground near to the surface as a result of irrigation practices of cultivated lands. The waterlogged bodies are extensively subjected to evaporation in arid regions, and

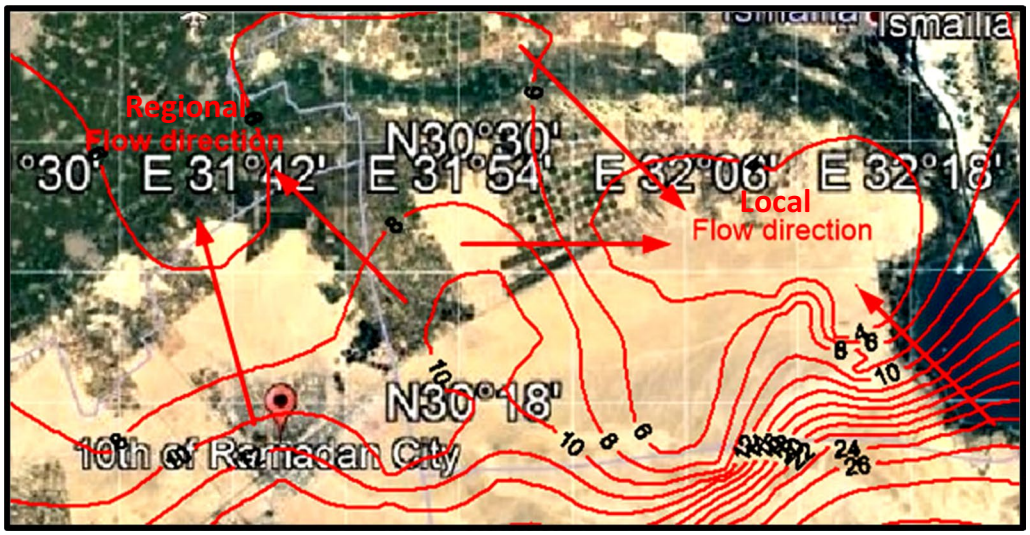

Fig. 4 Water table contour map of selected groundwater wells in the 10th RIR and neighboring areas in December 2005, displaying regional flow (from south to northwest) and local flow (from west to east) directions (Gad et al. 2015)

Table 1 Hydrogeological field data for several of the accessible water wells in the 10th RIR

Parameter	Well no				
	W24	W23	W25	W1	W28
Lat	30°18′0.216N	30°17′0.914N	30°18′0.822N	30°19′0.410N	30°19′0.458N
Long	31°47′0.540E	31°48′.543E	31°47′0.920E	31°47′0.847E	31°40′0.586E
Ground Elevation (m + msl)	102	106	102	96	94
Source Aquifer	Quaternary	Quaternary	Quaternary	Quaternary	Quaternary
Aquifer type	Leaky	Leaky	Leaky	Leaky	Leaky
Total Depth (m)	120	120	100	70	80
Depth to Water (m)	80	80	45	35	40 m
Temperature (°C)	28.5	28.3	30.8	28.9	28.5
pH	8.7	8.9	8.2	7.73	7.69
Ec (mS/cm)	6.37	6.12	2.6	2.05	2.58
TDS (mg/l)	5900	5720	3240	1880	2250

subsequently raising their salinity. The industrial sewage water from the factories of the 10th RIR, as well as the municipal sewage water from the urban zone, are discharged directly into three unlined oxidation ponds to the east of the mapped area (Fig. 5). The domestic wastewater from the urban areas is drained into oxidation pond No. 1, which estimated by volume of about 14.000 m^3/day. In addition, the domestic and industrial wastewater with an average flow of about 13.000 m^3/day is normally drained into oxidation pond No. 2. The drainage water of the heavy industries at the 10th RIR reaches the oxidation pond No. 3 with an average flow of about 25.000 m^3/day (Taha et al. 2004). Usually, all oxidation ponds are completely filled with wastewater, which is continuously overflows and drained to Wadi El-Watan. These effluents accumulate in the lowlands and are illegally used to irrigate newly reclaimed lands. The oxidation ponds at the 10th RIR contain untreated industrial and municipal sewage, causing recurring water pollution issues and being extremely polluting sources.

Materials and methods

Remote sensing and GIS data

The data employed in this study are generally in three formats: digital, non-digital, and descriptive data. The available digital data for constructing multi-temporal LU/LC thematic maps are the multi-temporal satellite images including Landsat 5 Thematic Mapper (TM), Landsat 7

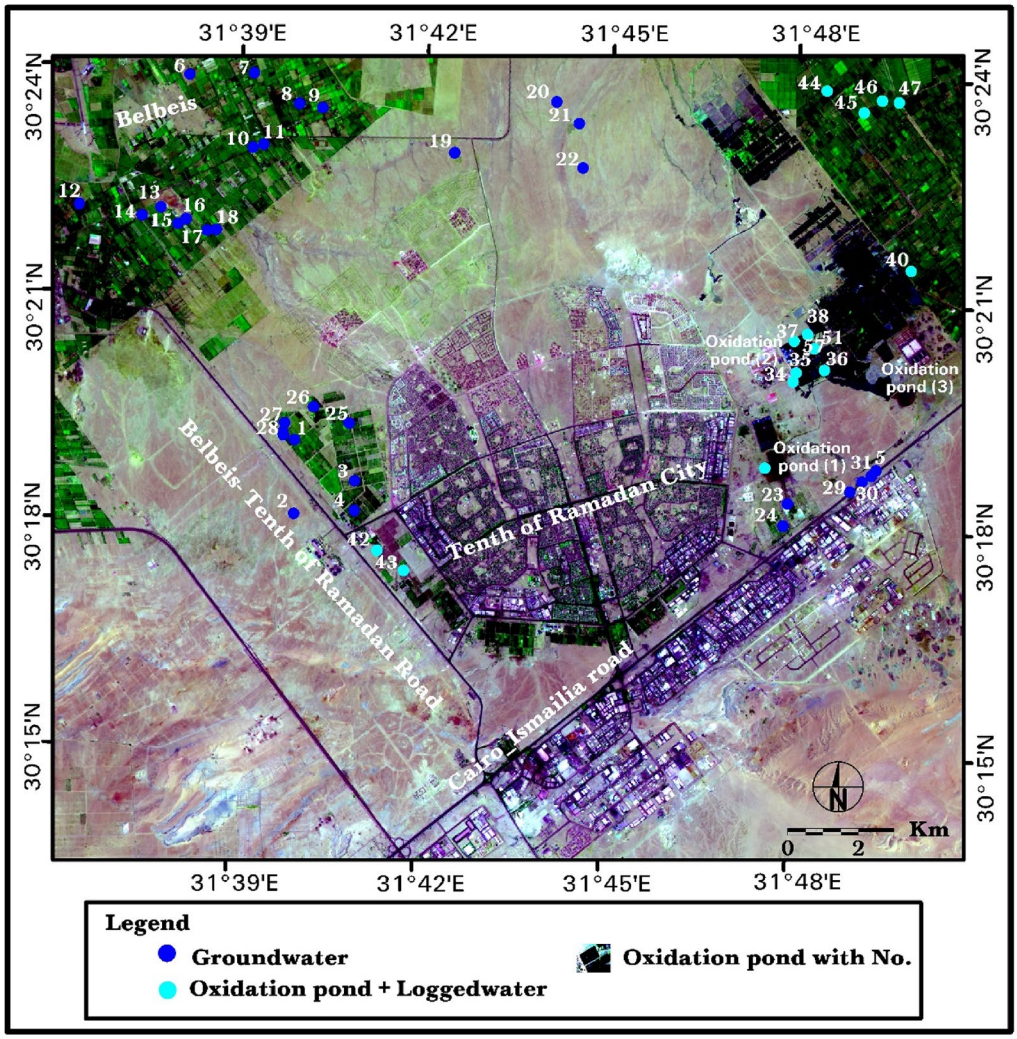

Fig. 5 Map showing the locations of the oxidation ponds and surface and ground water samples in the 10th RIR

Enhanced Thematic Mapper (ETM 7+), and Landsat 8 Landsat operational land imager (OLI) dated 1984, 2000, 2006 and 2017, respectively (Fig. 6). In addition, ASTER GDEM data was utilized to implement the terrain analysis and extract the drainage network to perform and calculate the qualitative and quantitative morphometric analysis of the flash flood hazards.

In the current study, all remotely sensed data were atmospherically, radiometrically, and geometrically corrected. To generate various kinds of LU/LC thematic maps, they used a range of image processing and enhancement techniques such as data fusion, indices, spatial filtering, contrast stretching, principal component analysis, image classification, and change detection. The Dark-Object Subtraction approach was used for atmospheric correction (Chavez 1996). RS techniques, such as selecting the best spectral reflectance bands to compare with other spectral wavelengths, were put to use in order to identify the best results for monitoring and assessing land degradation and hazard indicators. Additionally, the ideal digital image processing techniques are implemented to demarcate, appraise and map the multi-temporal RS data. To acquire primary data on LC and indicators of waterlogging and salt-affected soil hazards, spectral response arrays are used with multi-temporal and multi-spectral data of various LU classes. Furthermore, image enhancements, including best band combination, band rationing, principal component analysis (PCA), change detection, and the Maximum Likelihood Classification are implemented. These are utilized to create the extremely spectral resolution images required for diagnosing and monitoring waterlogging, soil salinization, and other environmental hazards between 1984 and 2017 (Fig. 7). The most appropriate band combination

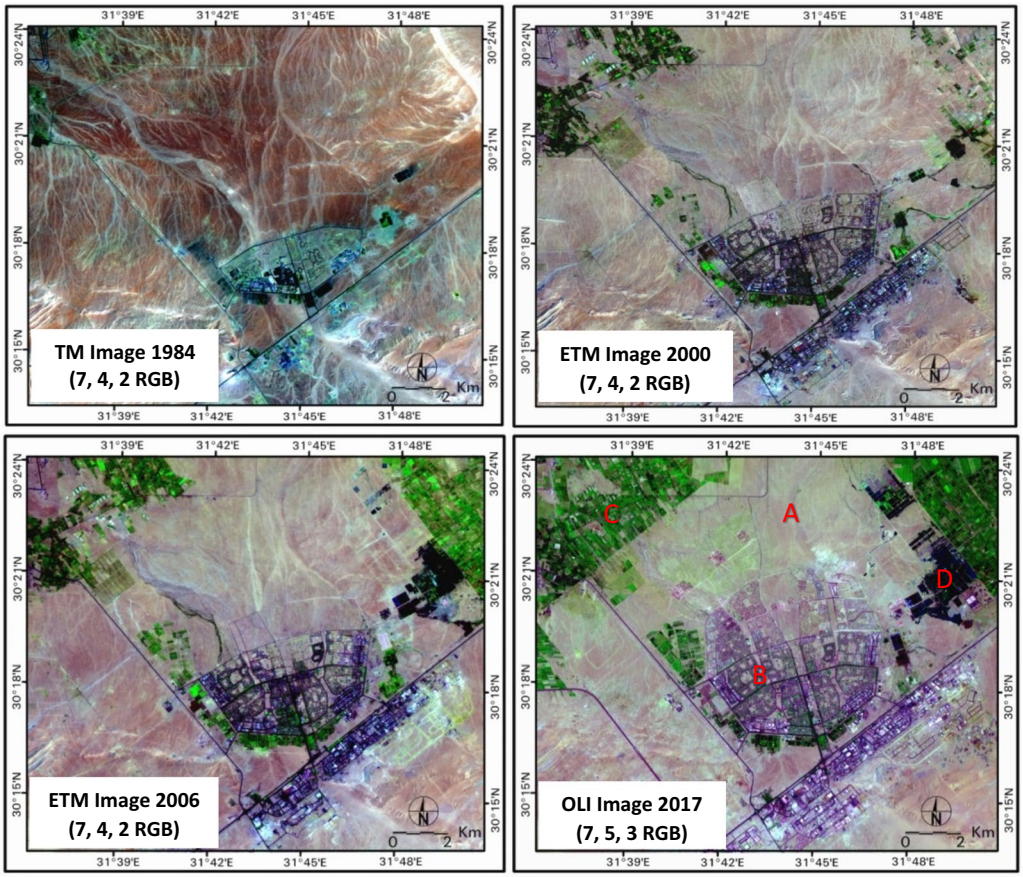

Fig. 6 Best band combination (7, 4, 2 RGB) for TM 1984, ETM 2000 & 2006, and (7, 5, 3 RGB) for OLI 2017 of 10th RIR exhibiting **A**: Bare lands class, **B**: Urban areas class, **C**: Vegetation class, and **D**: Oxidation ponds and waterlogging class

of the enhanced multi-temporal satellite data gives high contrast among LU/LC selected classes. To produce the spectral response curves of the specified main classes, RS data are presented and the spectrally homogenous zones of the different LU categories of 10th RIR are recognized. All image processing and constructed digital thematic maps were treated utilizing the ERDAS Imagine, ENVI, and ArcGIS software.

The non-digital data includes various kinds and scales of maps covering the study area including four topographic contour maps (namely; Belbeis, Enshas, El-Robaiky and Gabal El- Anqabiya sheets) for the Eastern Nile Delta of scale 1:50,000 (Egyptian Military Survey 1987) and the geologic map of Northeastern sheet of Egypt of scale (1:1,000,000) (Remote sensing Center, Academy of Scientific Research and Technology, Egypt, 1980).

Descriptive and fieldwork data

Many types of descriptive and fieldwork data were collected and inserted as attribute layers in the GIS such as, meteorological, hydrogeological, hydrological, and geologic data of the 10th RIR.

Estimation of morphometric parameters and flood hazard modeling

GIS tools have been shown to be useful for delineating and extracting stream networks, as well as assessing and managing the 10th RIR's flash flood hazard. Applying the Arc Hydro functions tools in ArcGIS Spatial Analyst in the current study enables mapping the drainage system of the 10th RIR as well as estimation of morphometric parameters (Table 2). It contains the output of a number of mathematical functions in ARC Hydro (Maidment 2002, Kumar et al. 2000, Zhang et al. 2009, Omran 2011, Rai et al. 2014, Arnous 2016, Arnous and Omer 2018, Arnous et al. 2020).

To assess the flood hazards ranking, hydrological, morphometric, and rainfall analyses were performed on the 10th RIR watershed. The DEM analyses are carried out using Arc Hydro functions in ArcGIS software to delineate the drainage network of the 10th RIR watershed and extract the morphometric parameters in order to

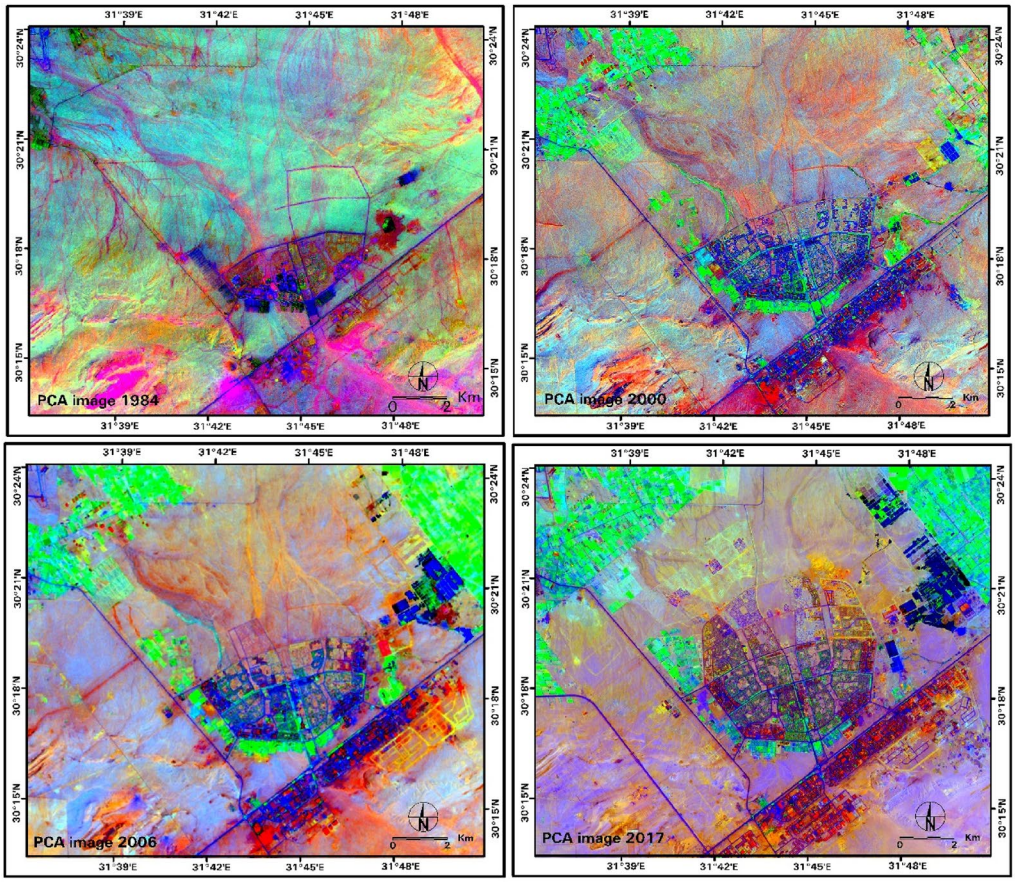

Fig. 7 PCA-enhanced multi-temporal Landsat images from the 10th RIR between 1984 to 2017, revealing the signatures of waterlogging, soil salinization, and other LU classes

Table 2 Morphometric parameters and their mathematical formula

Morphometric parameters	Formula	References
Stream frequency (F)	$F = N_u/A$	Horton (1945)
Stream density (D) km/km^2	$D = L_u/A$	Horton (1945)
Basin area (A) km^2	GIS software Analysis	Schumm (1956)
Circularity ratio (R_c)	$R_c = 4\pi A/P^2$	Strahler (1964), Miller (1953)
Weighted mean R_b (R_{bw})	$R_{bW} = \Sigma[R_b u: u + 1*(N_u + N_{u-1})]/\Sigma N$	Strahler (1952)
Overland Flow (OLF)	$OLF = 1/2D$	Horton (1945)
Basin relief (H)	$H = H_{Max} - H_{min}$	Hadley and Schumm (1961)
Basin length (L_b) km	GIS software Analysis	Schumm (1956)
Mean Gradient (MG)	$MG = H/L_b$	Strahler (1964)

estimate the flash flood hazards levels for the 10th RIR area. The morphometric parameters were estimated by analyzing various quantitative and qualitative aspects of the 10th RIR, such as stream order, stream frequency, bifurcation ratio, weighted mean bifurcation ratio, drainage density, drainage segment lengths, basin area and perimeter, basin ratio, basin elongation and circularity (Kumar et al. 2000, Arnous et al. 2011, Mondal and Gupta 2015, Arnous and Omer 2018). Finally, the weighted morphometric parameters for the basin data were statistically analyzed. By integrating the parameters of all scored thematic layers with GIS functions, an overlay operation was

used to evaluate the overlapped areas in order to delineate the flash flood vulnerable zones (Flash flood hazard model). The obtained integrated map is categorized into three flash flood hazard zones: high, moderate, and low.

Geo-hazards modeling and field verification

In order to create the integrated geo-hazards model of the 10th RIR, the current study uses GIS analysis and data integration to correlate the spatial distribution mapping of heavy metal pollution indicators in groundwater with the flood hazards zonation in the W. Gafra basin. To confirm the processed satellite data and determine the causes of land deterioration, a field survey was conducted. This survey included a sampling of water as well as GPS projection. Additionally, field checks have been carried out on the enhanced RS data.

Surface and groundwater data

On October 7, 2017, the samples were collected during a field excursion to the research area (Fig. 5). Chemical analyses are performed on samples of the available groundwater and surface water sources in the 10th RIR to identify their susceptibility to contamination by industrial wastewater discharges. Waters from wells, drains, and ponds in the 10th RIR were collected in acid-cleaned, tightly sealed polyethylene bottles, and then quickly transported to the Water Laboratory of the College of Agriculture, Suez Canal University, for vitro chemical examination. Waters were chemically examined for major ions and some trace element constituents following standard methods (APHA 1971). Major ions, Ca^{2+}, Mg^{2+}, Cl^{-}, HCO_3^{-}, and CO_3^{2-}, were analyzed by volumetric titration using a standard analytical method. The ions K+and Na+were measured using a flame photometer, whereas SO were measured using a spectrophotometer. Atomic absorption was used to identify the trace elements, which included Fe, Ni, Mn, Zn, Pb, Cu, and Co. Physico-chemical parameters, such as temperature, electric conductivity (Ec), and pH values, were measured in-situ using a thermometer, an Ec-meter, and a pH-Hanna pocket meter, respectively.The innovative aspect of this study is not the development of a novel methodology, but rather the approach for utilizing several tools in the data integration process to produce the final geo-hazards model. This concept is well represented by the flow chart (Fig. 8), which summarizes the approach and data utilized in the current analysis of the 10th RIR.

Results and discussion

LU/LC thematic datasets are significant sources for numerous applications, for instance socioeconomic studies, and environmental land degradation management and planning, and environmental impact appraisal. In the 10th RIR, the increasing population and economic activities growth have resulted in rapid industrial, agricultural and urban expansion in the last three decades. Consequently, timely and accurate mapping of LU/LC activities is often necessary to identify, monitor, analyze, and assess

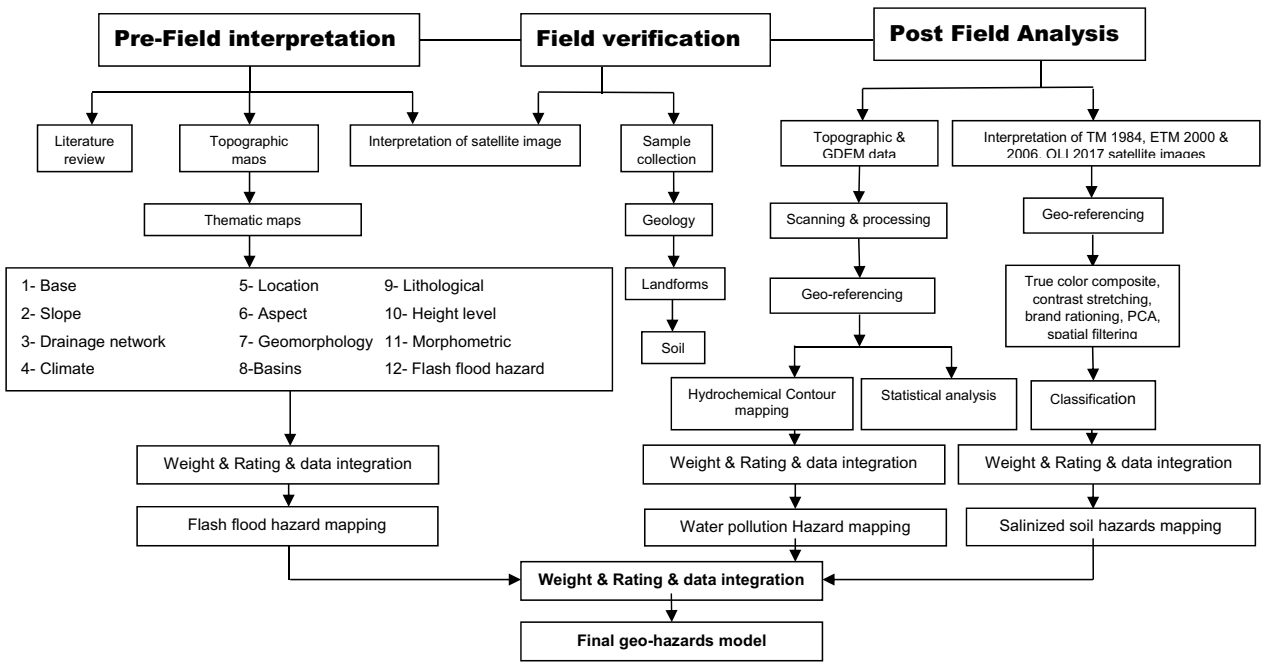

Fig. 8 Flow chart summarizing the methodology and information used in the current analysis of the 10th RIR

the environmental land degradation in the 10th RIR. Several methods for image processing and classification have been developed and applied in this study to construct multi-temporal LU/LC thematic maps for the 10th RIR complex landscape based on classified multi-temporal satellite observatory data.

Land use/land cover and land degradation analyses

The current study examines changes in the 10th RIR's land use/land cover classes caused by natural and anthropogenic activities using landscape metrics and environmental indicators of land degradation. Seven major classes; including vegetation, salt-crust, waterlogged, oxidation pond, urban zone, industrial zone and bare-land; are delineated. Additionally, fieldwork and verification are conducted for the chosen training spots to clarify the reasons for land degradation caused on by waterlogging, soil salinization, and other environmental hazards (Additional file 1: Fig. S1). The spectral pattern variations for waterlogged, salt-affected, vegetation and urban classes are extracted from satellite data and then normalized to the near infra-red (NIR) band in order to provide a visual comparison of class variation with time (Arnous and Green 2015; Arnous et al. 2015). The LU/LC thematic maps were prepared for the years 1984, 2000, 2006 and 2017. The different areas of each class reflect the evolutional changes in the LU/LC classes during 33 years (Fig. 9A–D).

The LU/LC class areas for each year are displayed in (Table 3). The classification results show that the main LU/LC classes in the years 1984, 2000, 2006, and 2017 in the 10th RIR were: the bare lands (85.44%, 61.99%, 53.29%, and 0.27); the bedrocks unit (66.41%, 11.9%, 4.06%, and 1.7%); and the W. Gafra (15.54%, 8.33%, 5.68%, and 1.68%); however, these classes have consistently decreased from 1984 to 2017. The salt areas increased from 1984 to 2017 by 0% to 0.72% respectively, the vegetation areas increased from 1984 to 2017 by 0.65% to 24.24%, and the industrial area increased by 7.6–13.9% during the period from year 1984 to 2017. The oxidation ponds, urban and waterlogged areas were increased (0.5–3.61%), (5.6–28.35%) and (0–2.04%) respectively during the period from 1984 to 2017.

When identifying and delineating the environmentally impacted sites in the 10th RIR, RS data and GIS tools offer an excellent substitute for traditional mapping techniques. LU/LC variations in the 10th RIR are identified through the analysis of multi-temporal data using GIS tools (Jensen 2004, Arnous and Green 2015, Arnous et al. 2017). The change detection analysis is used to track changes in the LU/LC classes of the 10th RIR from 1984 to 2017 (Table 3). The findings revealed that the 10th RIR is threatened by rapid and growing changes in LU/LC engendered by both natural and anthropogenic activities. The visual interpretation of the enhanced Landsat images showed that a number of factors, including population growth, developments in agriculture and economic sustainability, and hydrogeological and geological attributes, all had a significant influence on changes in LU/LC within the 10th RIR. The 10th RIR's natural resources are particularly susceptible to degradation as a result of these multiple functions.

Change detection of LU/LC can be classified as increasing or decreasing based on the impact of change and the criteria of land degradation hazards (Table 4). Agricultural activity changes (approximately 68.52 km^2) increased at a rate of + 2.07km^2/year from 1984 to 2017. This is due to agricultural development and an increase in population growth rate. Waterlogging areas are expanding at a rate of 0.16 km^2/year, covering approximately 5.4 km^2. The oxidation ponds grew by 0.27 km^2/year, totaling 9.19 km^2. Additionally, urban and industrial areas make up about 89.7 km^2 of the changes in residential LU. According to the annual rate of change, the LC of the 10th RIR landscape is significantly impacted by these activities in the study area.

The complicated hydrogeological setting brought about by the low hydraulic conductivity of top soils and the dispersion of surface industrial effluents, as well as LU misplanning and an inefficient strategy of industrial and land reclamation developments, particularly in desert fringe areas, are primarily responsible for spreading of soil degradation features in the 10th RIR landscape.

Identification of water pollution hazards

The pollution hazard expresses the impact of anthropogenic activities on groundwater quality, based not only on the extent of vulnerability, but also on the presence of potential pollution sources, which are dynamic factors. The severity of the impact is determined by the aquifer's vulnerability to contamination, the frequency of contamination, and the importance of groundwater resources (Lobo-Ferreira and Oliveira 1997).

Surface water geochemistry

Industrial sewage usually contains specific chemical compounds related to the nature of the industrial process. Most of the surface water examined, specifically

(See figure on next page.)

Fig. 9 Land use and land cover classes in the 10th RIR, displaying the areal distribution and the percentage of each LU/LC class in 1984 (**A**), 2000 (**B**), 2006 (**C**), and 2017 (**D**)

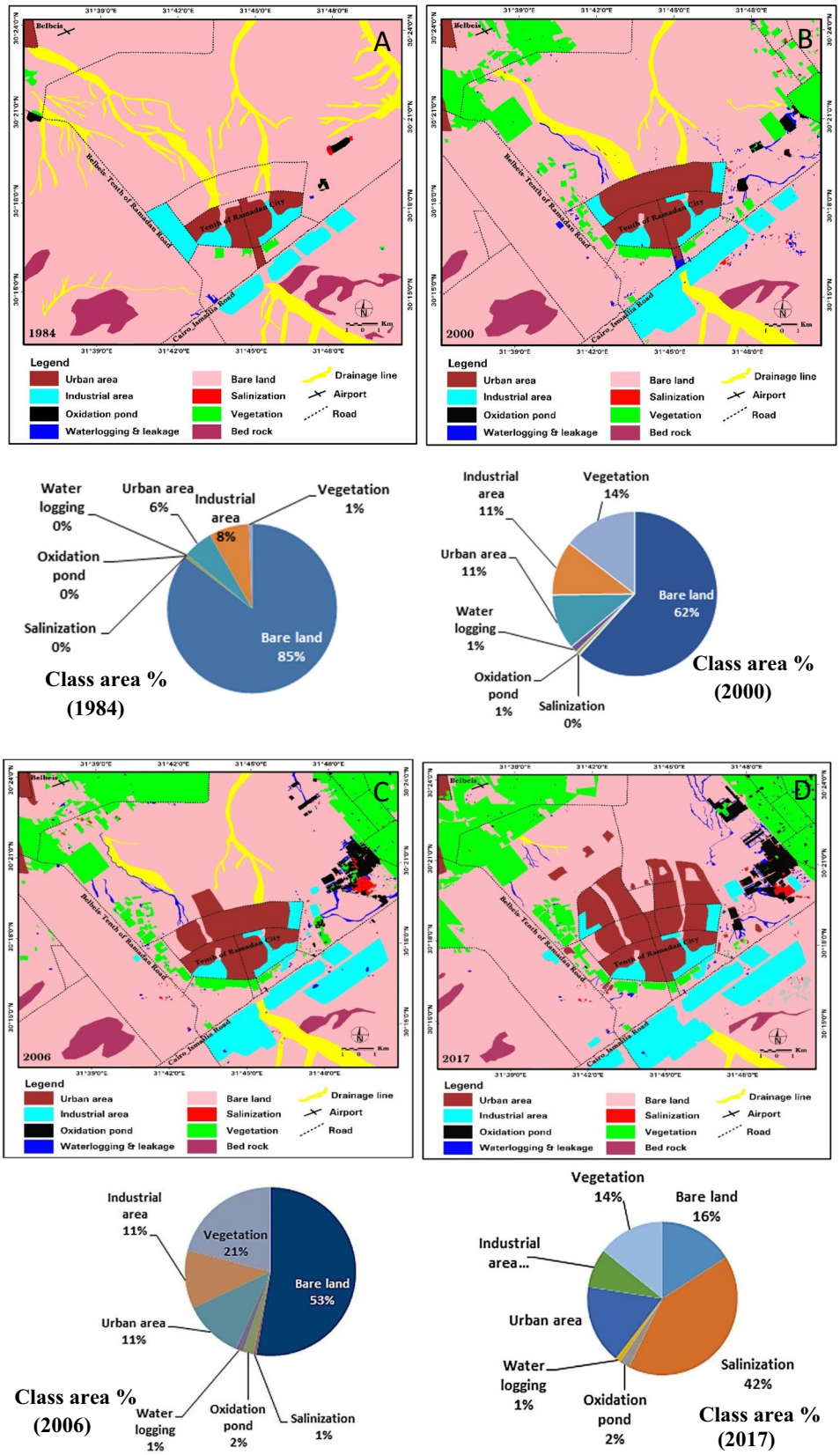

Fig. 9 (See legend on previous page.)

Table 3 The areas of LU/LC classes during 1984, 2000, 2006 and 2017 of 10th RIR

LU/LC classes	1984		2000		2006		2017	
	Km^2	%	Km^2	%	Km^2	%	Km^2	%
Bare land	208.9	85.4	157.0	62.0	162.0	53.3	78.5	0.3
Oxidation pond	1.3	0.5	1.8	0.6	6.1	2.1	10.5	3.6
Urban area	13.7	5.6	27.3	10.8	28.9	10.1	82.0	28.4
Industrial area	18.7	7.6	26.7	7.4	32.2	11.3	40.5	13.9
Waterlogging	0.2	0.0	3.4	1.4	3.9	1.4	5.6	2.0
Vegetation	1.6	0.7	36.4	14.3	60.4	21.2	70.1	24.2
Salinization	0.2	0.0	0.7	0.2	1.7	0.6	2.1	0.7
Wadi Gafra	38.0	15.5	21.1	8.3	16.2	5.7	4.9	1.7
Bed rocks unit	162.4	66.4	30.2	11.9	11.7	4.1	5.2	1.7

Table 4 The change detection statistics of the LU/LC classes in 1984, 2000, 2006 and 2017 of 10th RIR

LU/LC classes	1984–2017		2000–2006		1984–2000		2006–2017	
	Change in area (Km^2)	Rate of change (Km^2/year)	Change in area (Km^2)	Rate of change (Km^2/year)	Change in area (Km^2)	Rate of change (Km^2/year)	Change in area (Km^2)	Rate of change (Km^2/year)
Bare land	− 130.5	− 3.9	− 5.0	− 0.8	− 51.9	− 3.4	− 83.6	− 7.5
Oxidation pond	+9.2	+0.3	+4.4	+0.7	+0.5	+0.0	+4.3	+0.4
Urban area	+68.3	+2.1	+1.6	+0.3	+13.6	+0.8	+53.1	+4.8
Industrial area	+21.8	+0.6	+5.5	+0.9	+9.0	+0.5	+8.3	+0.7
Waterlogging	+5.4	+0.2	+0.5	+0.1	+3.3	+0.2	+1.7	+0.1
Vegetation	+68.5	+2.1	+24.0	+4.0	+34.8	+2.2	+9.7	+0.8
Salinization	+1.9	+0.1	+1.1	+0.2	+0.5	+0.1	+0.4	+0.0
Wadi Gafra	− 33.1	− 1.0	− 4.9	− 0.8	− 16.8	− 1.0	− 11.3	− 0.8
Bed rocks	− 157.2	− 4.7	− 18.5	− 3.1	− 132.2	− 8.3	− 6.5	− 1.1

in the oxidation ponds, has high trace elements contents (Table 5). They have serious impacts on human health; therefore, the present work paid more attention to defining the impact of oxidation ponds seepage into the adjoining groundwater bodies.

The hydrochemical analyses of the water samples collected from oxidation ponds and logged waters show wide variability from site to site due the interferences of several factors including: the source of industrial wastewater, the stagnant residence time, recharge rate to these water bodies, the influence of evaporation and the type of soil draining the water bodies.

The TDS values of the surface water have slightly increased from 220 mg/l to 2872 mg/l (Table 5). The high concentration of dissolved solids in the surface water of the 10th RIR is associated with high sodium content (Fig. 10), implying that evaporation directly impacts water salinity.

Calcium and Magnesium contents in surface water have similar distribution revealing the same behavior of both elements. They varied from 31 mg/l to 111 mg/l and from 10.9 mg/l to 43.7 mg/l, respectively (Table 5).

Sodium and chloride in surface water have the same rising content revealing the same behavior for both elements. They ranged from 27 mg/l to 1000 mg/l and from 27.9 mg/l to 1000.7 mg/l, revealing the effect of the evaporation process on surface water bodies in such an arid environment (Table 5).

The sulphate content of surface water ranged from 12 to 190 mg/l (Table 5). The dissolved detergents used in washing processes may be the source of sulphate in industrial wastewater.

The bicarbonate content of the 10th RIR's surface water ranged from 151.7 mg/l to 1215 mg/l (Table 5). The oxidation of organic matter enriching the industrial waste water may be the source of bicarbonate in the waste water.

Table 5 reveals that the pH, TDS, Ca, Na, K, HCO_3, Cl, Ni, Cu, and Fe of surface water exceeded the WHO (1996) permissible level. The maximum estimated

Table 5 Summary of chemical analyses of surface waters in 10th RIR

Parameter	Number of samples	Min	Max	Average	Standard deviation	Permissible ranges (WHO 1996)
pH Value	14	6.5	8.9	7.8	0.7	6.5–8.5
TDS (mg/l)	14	220.0	2872.0	936.1	822.5	1000
Ca (mg/l)	14	31.8	111.1	67.6	28.4	75
Mg (mg/l)	14	10.9	43.7	20.3	9.5	150
Na (mg/l)	14	27.0	1000.0	267.8	300.5	200
K (mg/l)	14	3.0	72.0	18.5	19.3	12
HCO_3 (mg/l)	14	151.7	1215.1	486.9	309.3	500
SO_4 (mg/l)	14	12.0	190.0	92.9	61.1	250
Cl (mg/l)	14	27.9	1006.5	255.4	310.8	250
Ni (µg/l)	14	0.4	133.5	34.8	40.5	20
Co (µg/l)	14	0.4	6.2	2.6	1.9	50
Pb (µg/l)	14	1.4	33.2	15.8	8.9	50
Cd (µg/l)	10	0.3	0.5	0.3	0.1	3
Cu (µg/l)	14	0.4	44.8	18.9	16.2	5
Zn (µg/l)	14	2.0	417.3	104.0	136.6	3000
Mn (µg/l)	14	4.2	349.7	98.6	108.2	500
Fe (µg/l)	14	31.2	4168.0	887.5	1292.9	300

concentrations for TDS (2892 mg/L), Ca (111 mg/l), Na (1000 mg/l), K (72 mg/l), HCO_3 (1215 mg/l), Cl (1007 mg/l), Ni (134 µg/l), Cu (45 µg/l), and Fe (4168 µg/l) surpassed the WHO (1996) acceptable limit. While the highest concentrations of Mg (44 mg/l), SO_4 (190 mg/l), Co (6.2 µg/l), Pb (33.2 µg/l), Cd (0.5 µg/l), Zn (417 µg/l), and Mn (350 µg/l) were found in the permissible range.

Cluster analysis is useful for categorizing water chemistry and characterizing the hydrochemical groups of specific populations that may be relevant in the environmental context (Suk and Lee 1999, Farnham et al.2000, Swanson et al. 2001). The R-mode dendrogram of trace metal variables in water from oxidation ponds in the 10th RIR is interpreted and statistically classified into two main clusters. The first cluster group (G1) contains only Fe, indicating its importance as a component of the Earth system (Fig. 11). The Fe content of surface water ranged from 31.2 g/l to 4168 g/l (Table 5). The second cluster group (G2) contains Mn, Zn, Co, Cu, Pb, and Ni, illuminating the source of industrial contamination.

Groundwater geochemistry of 10th RIR

Recently, industrial and agricultural activities, as well as natural processes, have had a significant impact on the geochemistry of groundwater in the 10th RIR. The 10th RIR fully recognizes three major LU classes: oxidation ponds to the east, cultivated lands to the northwest, and the urban areas and surrounding bare lands in the middle of the mapped area (Fig. 9D). Groundwater beneath each of the aforementioned LU classes has a distinct chemical pattern that reflects the impact of past activities and/or natural processes.

The oxidation ponds in the northeastern zone serve as a surface reservoir for industrial waste water drained from various factories in the industrial sector of the 10th RIR. Because of the rapid increase in industrial activities and the associated resident population growth, pollutants may have a severe impact on groundwater (El-Sayed et al. 2012). Previous geophysical surveys show a decrease in resistivity values around the oxidation ponds, indicating wastewater infiltration down to 15 m depth (Attwa et al. 2013). The stored wastewater is likely to infiltrate downward and contaminate the shallow aquifer, resulting in geochemical changes in the composition of groundwater. Seepage from oxidation ponds and the expansion of cultivated lands that have been watered with wastewater both produce dangerous environmental threats (Khalaf and Gad 2015). Groundwater beneath both oxidation ponds and irrigated lands by untreated sewage water in the northeastern zone has high TDS values and is enriched in Na, SO_4, and Cl (Fig. 12).

The pH of the groundwater in the 10th RIR ranged from 7.3 to 8.9, with an average of 8.03 (Table 6). In general, the pH values gradually increase towards the northwestern cultivated zone of the mapped area. The local farmers illegally use the industrial wastewater of the 10th RIR in irrigation practices. A significant decrease in pH values is recorded in the northeastern zone of the study

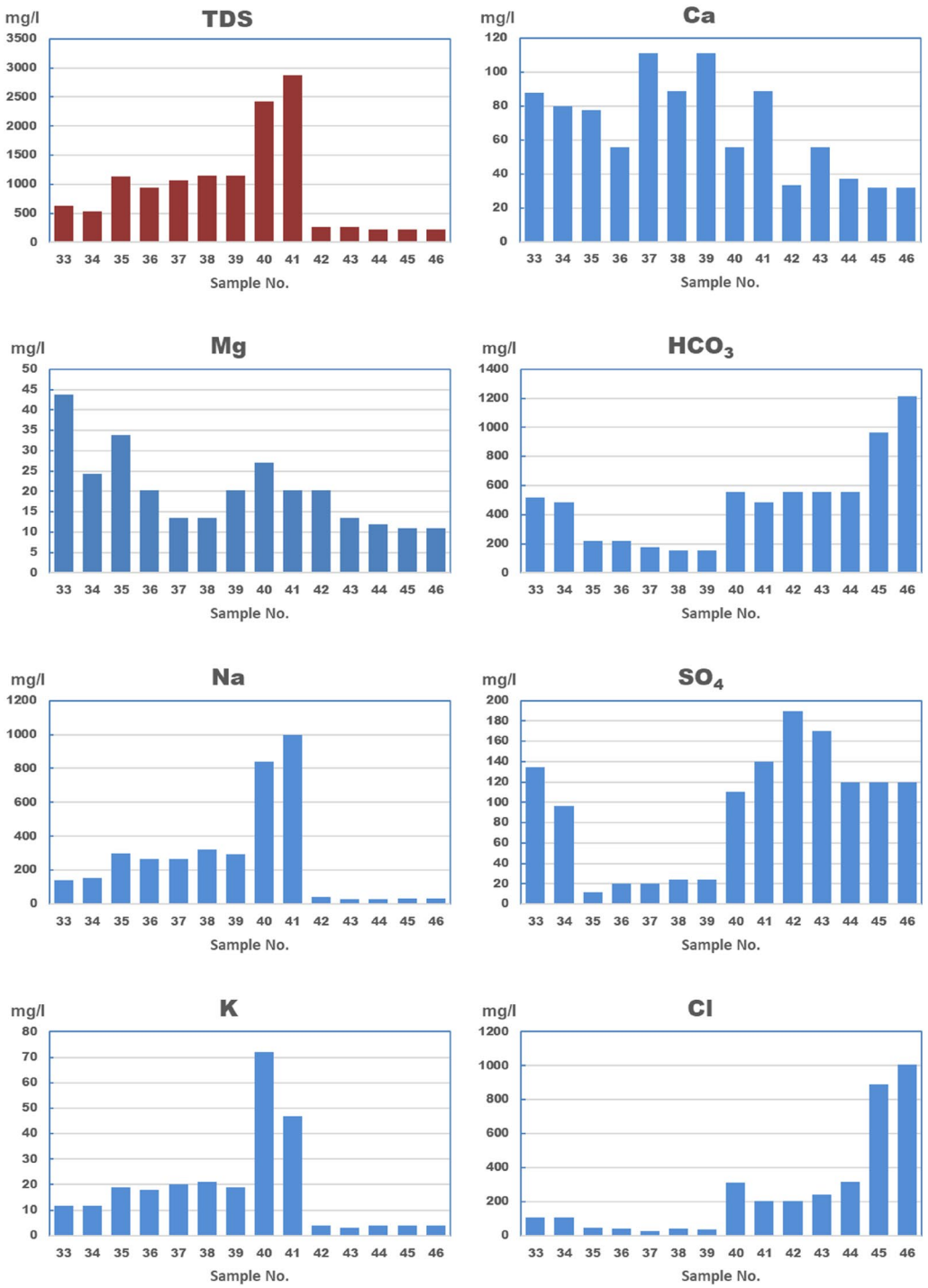

Fig. 10 Distributions of major ions in surface water of the 10th RIR

area, which may be attributed to the impact of oxidation pond reservoir leakage into the undelaying shallow aquifer (Fig. 12).

Groundwater TDS levels in the 10th RIR ranged from 128 mg/l to 6700 mg/l, with an average of 2290 mg/l (Table 6). TDS values increase in the northwestern and middle zones of the mapped area and decrease in the northeastern zone (Fig. 12). The groundwater flows from south to north and northwest (Fig. 4), which may confirm that TDS increases throughout the flow path. The

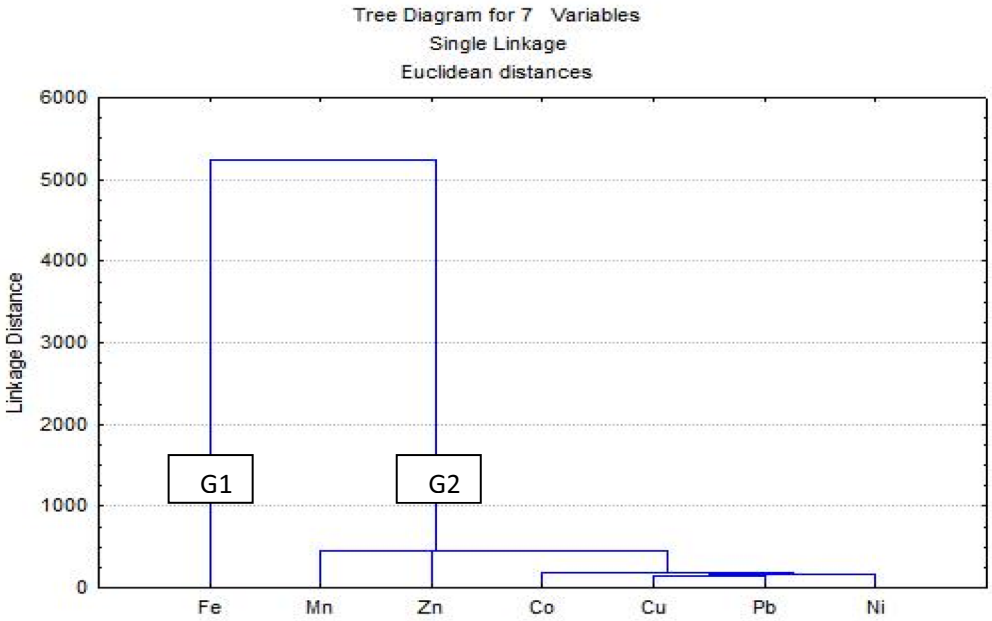

Fig. 11 Grouping discrimination in the cluster analysis of trace metal contents in surface water and oxidation ponds at the 10th RIR

Pleistocene leaky aquifer at the northwestern end of the flow path, which entirely supplies the irrigated lands in the northwestern and middle zones, may be principally responsible for the excessive TDS levels in those zones. The existence of oxidation ponds throughout the regional flow path suggests that industrial wastewater leakage from oxidation ponds has increased the salinity of groundwater in the middle zone.

The sodium content of groundwater in the 10th RIR varies greatly, ranging from 240 mg/l to 1850 mg/l (Table 6). The northwestern section of the study area has higher Na values due to the impact of high sodium returned flow irrigation water and washing of the salinized sodic soils (Fig. 12).

Calcium levels in the study area's groundwater ranged from 22.2 to 533.3 mg/l (Table 5). Ca values rise in the northwestern zone toward cultivated areas and fall in the northeastern zone (Fig. 12).

Mg levels in the study area's groundwater range from 2.5 to 527 mg/l (Table 6). Mg concentrations rise in the west around the cultivated area and fall in the south of the 10th RIR (Fig. 12).

Cl levels in the study area's groundwater range from 113 to 3593.17 mg/l (Table 6). Because of soil salinization and returned flow irrigation wastewater, the Cl value rises in the northwest zone (Fig. 12).

In the 10th RIR, SO_4 levels in groundwater range from 12 to 1027 mg/l (Table 6). The SO_4 value in the northeastern cultivated zone rises due to the impact of returned flow irrigation wastewater and leakage from nearby oxidation ponds, respectively (Fig. 12).

The bicarbonate content of groundwater in the study area ranges from 106 mg/l to 556 mg/l (Table 6). The bicarbonate value rises in the study area's northwestern corner (Fig. 12). The anomalous HCO_3 content at this location could be attributed to the impact of cultivation processes caused by the oxidation of organic matter enriching agricultural soils.

Table 6 reveals that the maximum estimated concentrations for TDS (6700 mg/l), Ca (2250 mg/l), Mg (528 mg/l) Na (1850 mg/l), K (78 mg/l), HCO_3 (1037 mg/l), SO_4 (1028 mg/l), Cl (3593 mg/l), Ni (265 µg/l), Co (265 µg/l), Cd (31 µg/l) and Fe (490 µg/l) surpassed the WHO (1996) permissible limit. While the highest concentrations of Pb (31 µg/l), Cu (3.8 µg/l), Zn (99 µg/l), and Mn (14 µg/l) were found in the permissible range.

Factor analysis is used to categorize the likely pollution variables affecting the groundwater in the 10th RIR area. The R-mode dendrogram of trace metal variables in groundwater from the 10th of Ramadan area is divided into three major clusters (Fig. 13). The first cluster (G1) has Fe as a main component; the second cluster (G2) has Ni; and the third cluster has Mn, Zn, Pb, Cu, and Co, which may indicate the impact of industrial wastewater. The presence of Ni in a single group may indicate that it has a higher mobility along the groundwater flow path than the other trace element components.

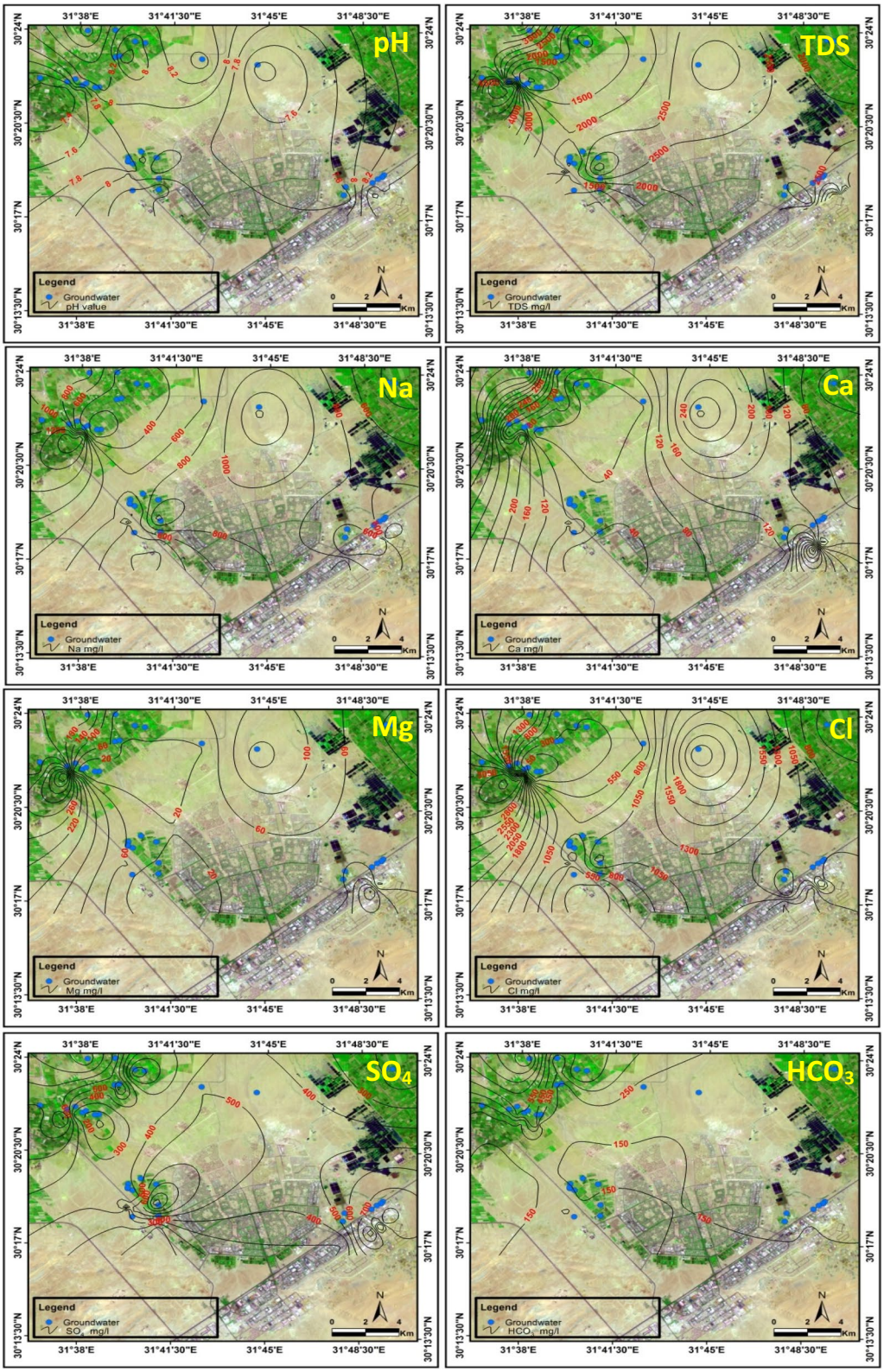

Fig. 12 Spatial distributions of major ion abundances in groundwater from the 10th RIR

Table 6 Summary of chemical analyses of groundwater in 10th RIR

Parameter	Number of samples	Min	Max	Average	Standard deviation	Permissible ranges (WHO 1996)
pH Value	32	7.3	8.9	8.0	0.4	6.5–8.5
TDS (mg/l)	32	128.3	6701.0	2289.6	1837.5	1000
Ca (mg/l)	32	10.0	2250.0	191.0	154.4	75
Mg (mg/l)	32	2.5	527.9	71.3	67.8	150
Na (mg/l)	32	188.0	1850.0	618.2	462.1	200
K (mg/l)	32	1.0	78.2	16.7	18.9	12
HCO_3 (mg/l)	32	88.0	1037.1	269.9	196.3	500
SO_4 (mg/l)	32	12.0	1027.8	419.2	318.2	250
Cl (mg/l)	32	102.6	3593.1	919.4	1001.4	250
Ni (µg/l)	19	0.4	265.0	29.2	83.1	20
Co (µg/l)	19	0.4	265.0	15.8	60.4	50
Pb (µg/l)	20	2.7	30.8	9.0	7.5	50
Cd (µg/l)	15	0.3	30.8	6.4	10.0	3
Cu (µg/l)	15	0.4	3.8	0.9	1.1	5
Zn (µg/l)	20	0.6	98.6	15.9	22.8	3000
Mn (µg/l)	20	0.6	13.7	3.5	3.4	500
Fe (µg/l)	20	1.0	490.4	131.3	156.4	300

The movement of trace metals is primarily governed by their relative mobility through the unsaturated zone. The majority of trace metals in groundwater travel as complex compounds with major ions. As a result, elements that are incapable of forming dissolvable complex compounds are extremely difficult to move in water (Shvartsev et al. 1975). Ren et al. (1989) stated that in arid environments, Cu, Pb, Ag, Mn, and Zn have relatively high immobility and thus have a low ability to migrate in water systems. El-Rayes (2010) asserts that while Mo, Ni, and Zn are highly mobile, Fe, Pb, Cr, and Mn are stationary elements. The movement of trace metal leachate through the unsaturated zone revealed that Sr leached faster than Fe along the soil profile (Hussien et al. 2017).

The mean average nickel content in the groundwater of the 10th RIR is within normal limits, with the exception of three samples taken beneath the cultivated zone in the northwest, where nickel levels are higher than allowed (Fig. 14). The primary source of nickel in the northwestern parts of the study area could be the returned flow irrigation wastewater. Chemical analyses of groundwater in the study area show that Co values rise in the eastern and southeastern parts of the study area, closer to the oxidation ponds and industrial zone (Fig. 14). Zn values increase in central parts and decreases towards the northern part of the 10th RIR (Fig. 14). Mn content varies between 0.6 and 13.7 µg/l (Table 6). Mn value increases via the eastern zone toward the oxidation ponds due to seepage of industrial effluent into groundwater (Fig. 14). Lead content in groundwater varied between 2.7 and 30.8 µg/l (Table 6). Lead value increases in northeastern part due to seepage from oxidation pond and decreases via southern zone (Fig. 14). Copper content varies between 0.4 and 3.8 µg/l (Table 6). Copper values increase at the central and eastern parts toward industrial and oxidation ponds zones due to seepage of industrial effluent (Fig. 14). Cadmium content varies between 0.3 and 30.8 µg/l (Table 6). Cadmium values rise in the northeastern and northwestern parts of the 10th RIR while falling in the south (Fig. 14). Cadmium in groundwater in the study area could be attributed to agricultural activities such as the use of cadmium-rich phosphorus fertilizers, and also seepage from oxidation ponds.3.2.3 Groundwater pollution hazards mapping of 10th RIR.

Because of the high population growth rate and large amounts of industrial wastewater discharge, the groundwater of the 10th RIR's shallow aquifer is highly vulnerable to pollution. The multivariate pollution weighted maps for each heavy metal are combined and classified based on the maximum allowable level of heavy metals in water. Thematic maps are created and then converted to raster or vector format so that they can be easily combined with ArcGIS' Spatial Analyst tool (Krishnamurthy et al. 1996, Saraf and Choudhury 1998, Srinivasa Rao and Jugran 2003, Naghibi et al. 2015, Arnous and El-Rayes 2013, Arnous 2016, El-Rayes et al. 2017). Furthermore, various GIS tools such as visualization, spatial query, integration, analysis, and predictions were used to create

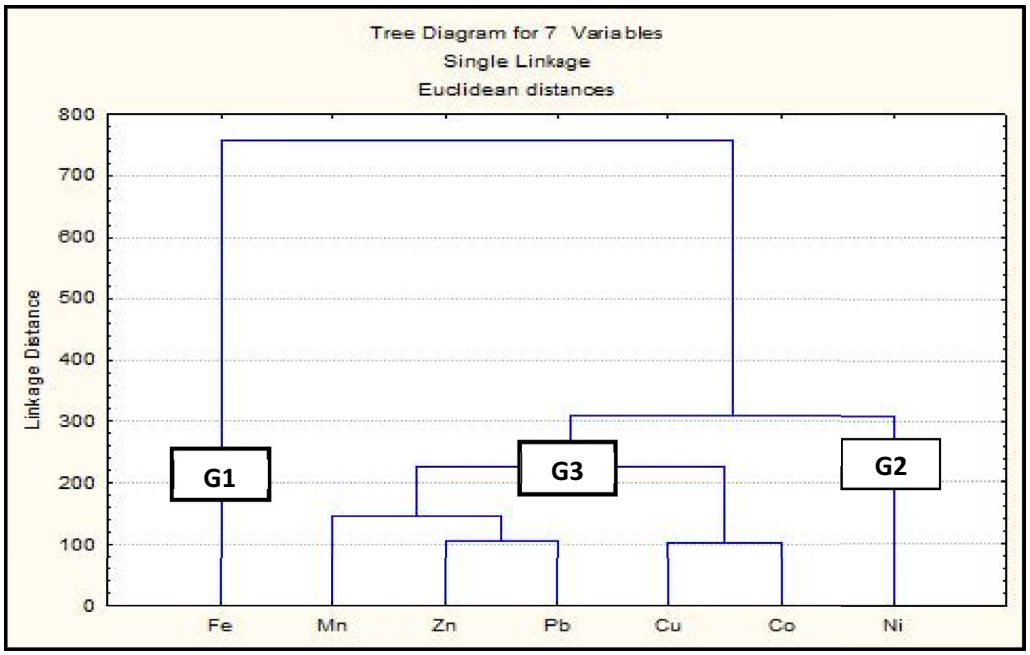

Fig. 13 Grouping discrimination in the cluster analysis of trace metal contents in groundwater at the 10th RIR

distribution maps of various chemical species affecting the pollution hazard. The groundwater pollution potentiality maps.are combined with the arithmetic overlay to identify areas most susceptible to pollution. The pollution risk map produced shows that the groundwater of the 10th RIR is highly vulnerable to pollution induced by oxidation pond and industrial wastewater leakage (Fig. 15). The resulting integrated potential pollution risk map is an excellent tool for decision makers concerned with groundwater protection and development. The present work entails creating a digital database for the 10th RIR.

Flash flood hazards mapping of 10th RIR.

When it rains heavily, flash flooding occurs on saturated or dry soil with low permeability. Climate fluctuations and extreme weather events are signs of climate change manifestation. In Egypt, there were severe weather events such as the recurrence of flash floods in the Fifth Settlement of East Cairo as a result of heavy rainfall in April 2018 (Kotb 2019), February and March 2020, and October 2022. Flash floods are among the natural disasters that cause the most human deaths and property destruction. Runoff accumulates in gullies and streams, and when they join to form larger volumes, they frequently form a fast-flowing front of water and debris. The purpose of this research is to estimate the flash flood hazards rank of the 10th RIR.

The W. Gafra basin drains the 10th RIR watershed and cuts through the main industrial and urban extension of 10th Ramadan city. Ten variables are represented as layers in the flood hazards model. Basin area, stream frequency, drainage density, basin circularity, weighted mean bifurcation ratio, overland flow, mean gradient, rainfall, infiltration, and circularity ratio are all contributing factors (Table 7). Based on the contributing factors related to geometry and morphometric parameters of the included basins, a general flood hazards model has been outlined. The drainage network characterization of the 10th RIR basins is quantitatively analyzed in terms of stream order, stream number, and stream length, length of overland flow, and bifurcation ratio, as described by Horton (1932, 1945), Strahler (1952, 1958), and Schumm (1956). These characteristics include basin shape, stream frequency, relief ratio, and drainage density. The flash flood hazards are primarily related to parameter values that are statistically analyzed using a simple statistical method (Arnous et al. 2011, Arnous and Green 2011, Arnous and Omar 2018). Based on the attributes of morphometric parameters and their potential level of hazard, each parameter is classified into three categories. The parameters are then divided into three hazards-level intervals. Various scaled scores regarding their significance to flood hazards are given in order to estimate the flood hazard rank (Table 8). An overlay process evaluates the crossed areas using score summation, resulting in a score degree for each area.

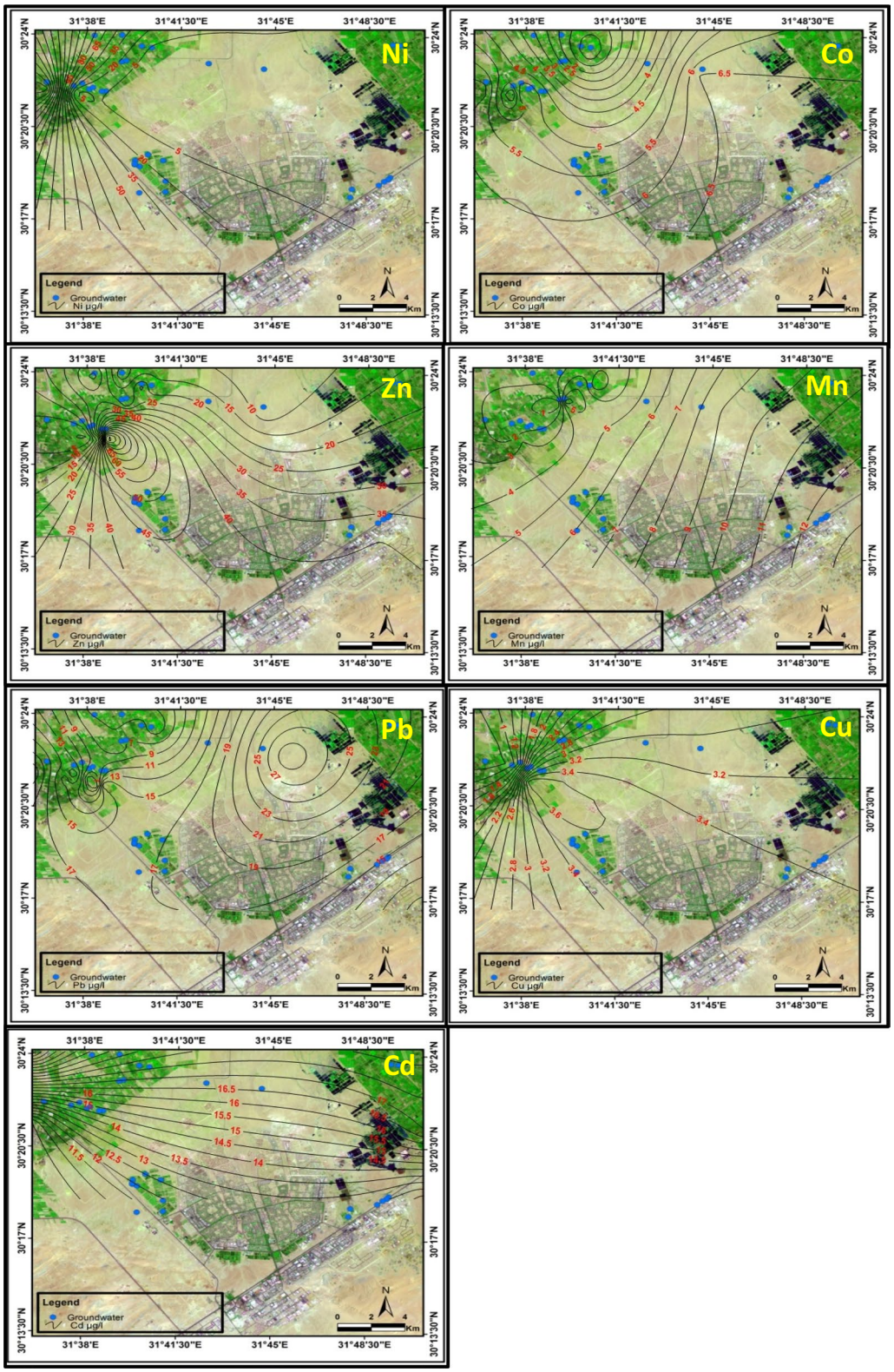

Fig. 14 Spatial distributions of trace metals abundances in groundwater from the 10th RIR

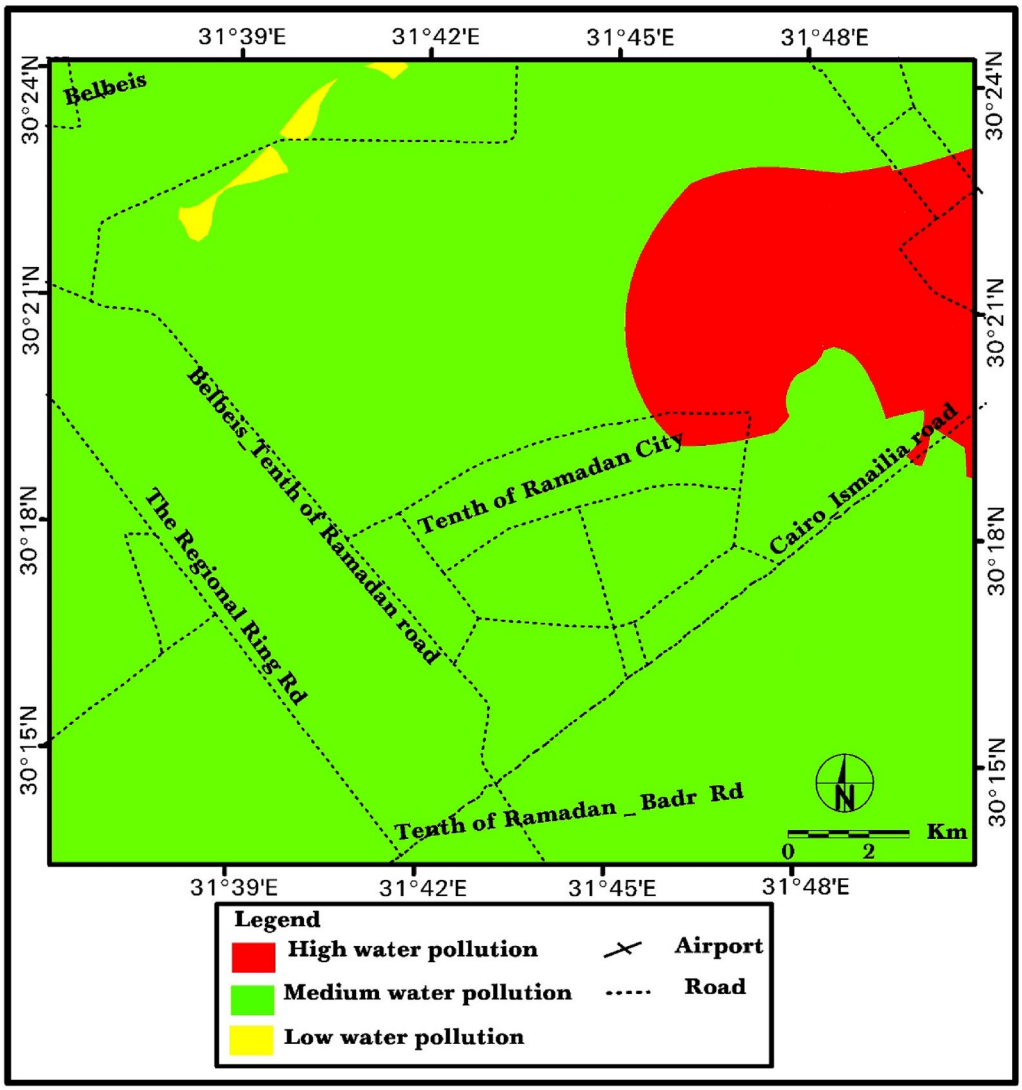

Fig. 15 Integrated potential water pollution risk map with risk rankings in the 10th RIR

To create a perfect map, the results are classified into three flood hazard susceptibility categories: low, moderate, and high ranks. The 10th RIR's final map of flood risk ranks (Fig. 16) demonstrates that sub-basins 1, 4, and 5 have high ranks of flooding risk, while sub-basins 2, 7, and 8 are thought to have moderate ranks of flooding risk. However, the rank of flooding is low in sub-basins Nos. 3, 9, and 10. The obtained results suggest that the 10th RIR is susceptible to high rank flash floods. Therefore, it is strongly advised to implement some mitigation strategies in order to lessen the severe effects of flash hazards on the current industrial and urban infrastructure and conserve floodwater for local uses.

Integrated geo-hazards mapping of 10th RIR.

The mapping, analysis, and integration of geospatial data to support environmental decision-making are the most significant applications of geospatial tools. To identify the most likely locations for groundwater contamination (Fig. 15) and flash flood hazards in the 10th RIR (Fig. 16), the present work uses GIS analysis and data integration to correlate the spatial distribution mapping of heavy metal pollution indicators in groundwater with the flood hazard zonation in the W. Gafra basin. This results in the creation of the geo-hazards risk map of the 10th RIR (Fig. 17). The 10th RIR's geo-hazards map was divided into three hazards categories, including high flash flood hazardous areas that are geospatially distributed in the southern parts of the W. Gafra basin and the

Table 7 Data of morphometric parameters of Wadi Gafra basin, 10th RIR

Basin No	u	N_u	L_u (Km)	R_{bw}	R_b	A (Km^2)	F	D	OLF	P	ML (Km)	R_c	R_e	H (m)	MG	Rf (m^3/y)	R_r	R_o
1	6	1604	1107.0	4.2	4.2	423.0	3.8	2.3	1.2	166.0	40.5	0.2	0.0	171.5	4.2	621.0	4.2	1073.0
2	6	1028	770.0	4.0	4.0	298.0	3.4	2.2	1.1	70.0	29.5	0.8	0.3	88.5	3.0	635.0	3.0	499.0
3	7	1518	1091.0	4.6	4.6	419.0	3.6	2.3	1.2	79.0	33.0	0.8	0.0	174.5	5.2	882.0	5.3	1.4
4	4	53	42.0	3.6	3.7	12.3	4.3	2.5	1.2	20.0	5.3	0.4	0.1	24.0	4.5	1320.0	4.5	12.0
5	4	30	17.0	2.9	3.0	7.1	4.2	2.5	1.2	16.0	3.5	0.3	0.2	13.0	3.7	1500.0	3.7	0.6
6	4	64	41.0	3.7	3.8	17.1	3.7	2.3	1.2	27.0	8.8	0.3	0.1	31.5	3.5	1700.0	3.6	36.0
7	4	110	74.0	4.4	4.4	29.0	3.8	2.3	1.2	36.0	9.5	0.3	0.1	42.5	4.5	688.0	4.5	36.7
8	4	29	20.9	2.8	2.9	8.2	3.5	2.3	1.1	14.0	5.1	0.5	0.2	27.5	5.4	700.0	5.4	0.3
9	5	217	14.3	3.7	3.8	54.5	4.0	2.4	1.2	48.0	14.3	0.3	0.1	45.0	3.1	747.0	3.1	18.0
10	5	167	113.3	3.7	3.7	43.8	3.8	2.3	1.2	46.0	12.9	0.3	0.1	48.0	3.7	882.0	3.7	11.4
Gafra Main	7	5098	4377.0	4.2	4.2	1491.0	3.4	2.2	1.2	363.0	78.4	0.1	0.1	223.5	2.8		2.9	

u: Stream order, N_u: Total number of streams of order u, L_u: Total length of stream, R_{bw}: Weighted mean, $R_b \rightarrow R_b$: Bifurcation ratio, A: Basin area, F: Stream frequency, D: Stream density, OLF: Overland flow, P: Basin perimeter, ML: Basin maximum length, R_c: Basin circularity ratio, R_e: Basin elongation, H: Difference in elevation, MG: Mean gradient, Rf: Rainfall

Table 8 Flash flood hazard weight numbers of the studied drainage basins, 10th RIR

Basin No.	Flash flood scores based on										Total hazard score
	F	D	A	R_c	R_{bw}	OLF	MG	Rf	INF	R_o	
1	2	2	3	3	1	2	2	1	2	3	21
2	1	1	2	1	2	3	1	1	2	2	6
3	1	1	3	1	1	3	3	1	2	3	19
4	3	3	1	3	2	1	2	2	3	1	21
5	3	3	1	3	3	1	1	3	3	1	22
6	1	1	1	3	2	3	1	3	3	1	19
7	2	2	1	3	1	2	2	1	2	1	17
8	1	1	1	2	3	3	3	1	2	1	18
9	1	1	1	3	2	1	1	1	2	1	14
10	1	1	1	3	2	2	1	1	2	1	15

western parts of the 10th of Ramadan City. Additionally, the salinized soil zones are seen as geospatially restricted areas, especially in the eastern zone of the 10th of Ramadan City and/or near the oxidation ponds. Furthermore, vast areas of highly polluted groundwater exist beneath industrial, urban, and oxidation pond zones. The created geo-hazards map will be helpful for the decision-makers to avoid the prevalent hazards that endanger the long-term development of the 10th RIR.

Mitigation measures for sustainable development of 10th RIR.

The application of geological engineering principles to reduce or avoid the effects of naturally occurring geo-hazards is known as geo-hazard mitigation. However, geo-hazards continue to have a significant impact on the economy and society. If they are identified, they may be avoided or prevented to varying degrees. The high flash flood hazard zone is located in the southwestern part of the 10th RIR, while the high groundwater pollution hazard zones are located in the northern part of the 10th RIR. The polluted hazard zone is primarily located near industrial and urbanized zones, which are the heart of economic development for the 10th RIR. As a result, priority should be given in these zones to reducing or controlling the rate of groundwater pollution through conservation planning. The conservation planning should take into account preventing industrial wastewater leakage into the underlying shallow aquifer. Both oxidation ponds and returned flow irrigation water are the main sources of that kind of leakage.

Mitigation measures can be used to protect industrial and urban zones from the severe impact of flash flooding. In management planning, priority should be given to implementing flash flood protection tools, such as

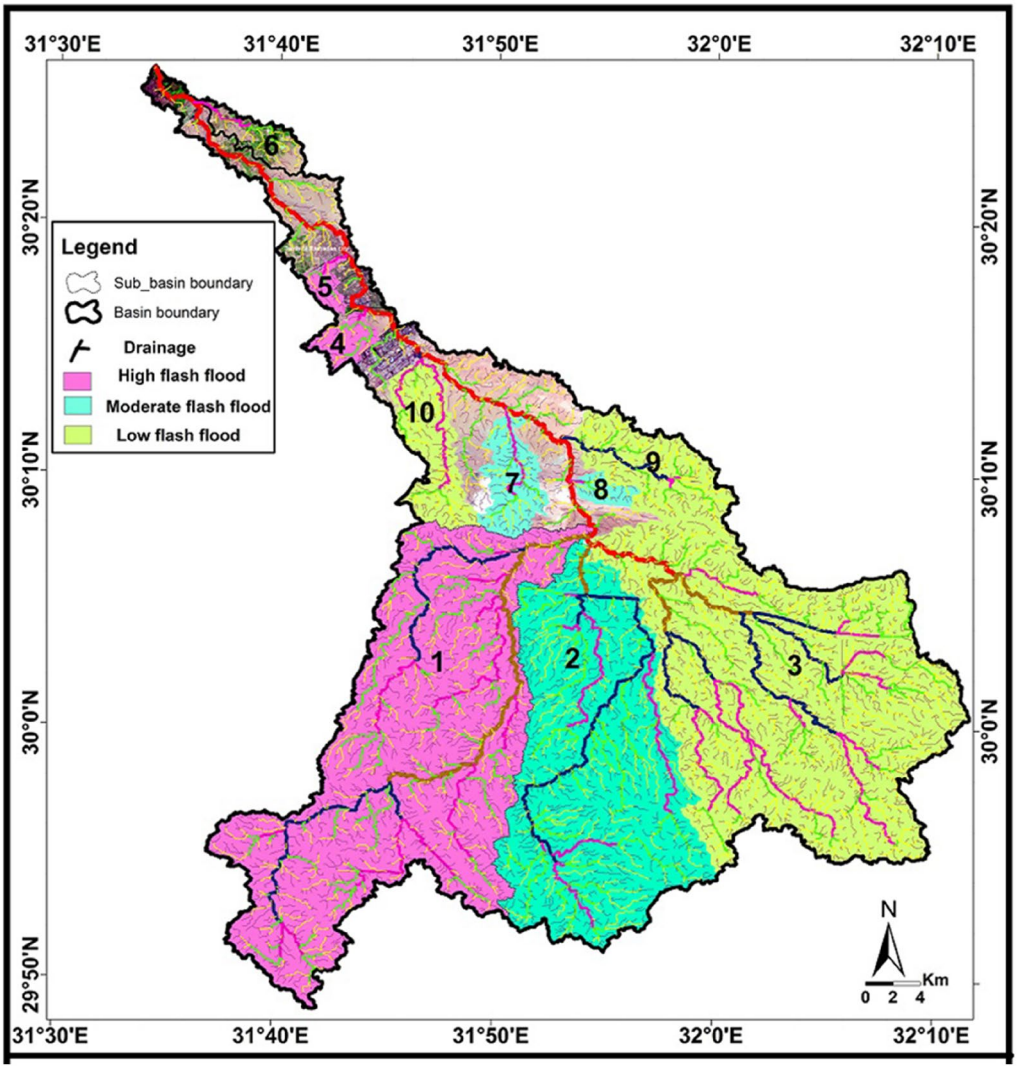

Fig. 16 Integrated flood hazard risk map based on morphometric indicators of the Wadi Gafra basin with risk rankings in the 10th RIR

low-cost flood control techniques, along the sub-basins of high flooding hazards rank.

The current study advised decision makers to implement the following mitigation measures to avoid the hazardous consequence of the present environmental difficulties within the 10th RIR for any future sustainable development planning activities:

- Land use planning should be done by adopting sustainable scenarios and policies in order to avoid the negative effects of humans and nature on the environment.
- Using some mitigation techniques to lessen the effects of flash hazards on the existing industrial and urban infrastructure and to keep floodwater for local use. The construction of hydraulic structures like storage dams, cisterns, and retardation dams along the sub-basins with a high rank of flooding is extremely important (Fig. 17).
- Priority should be given to conservation planning in order to slow down or stop the rate of groundwater pollution. Groundwater can be protected from pollution by lining oxidation pond bottoms with impervious material such as clay layer and treating irrigation wastewater before application as well.

Conclusions

The results of the current study indicate that leaks from oxidation ponds and irrigation water returned-flow that is supplied by industrial wastewater as a source are very likely to contaminate the groundwater of the 10th RIR.

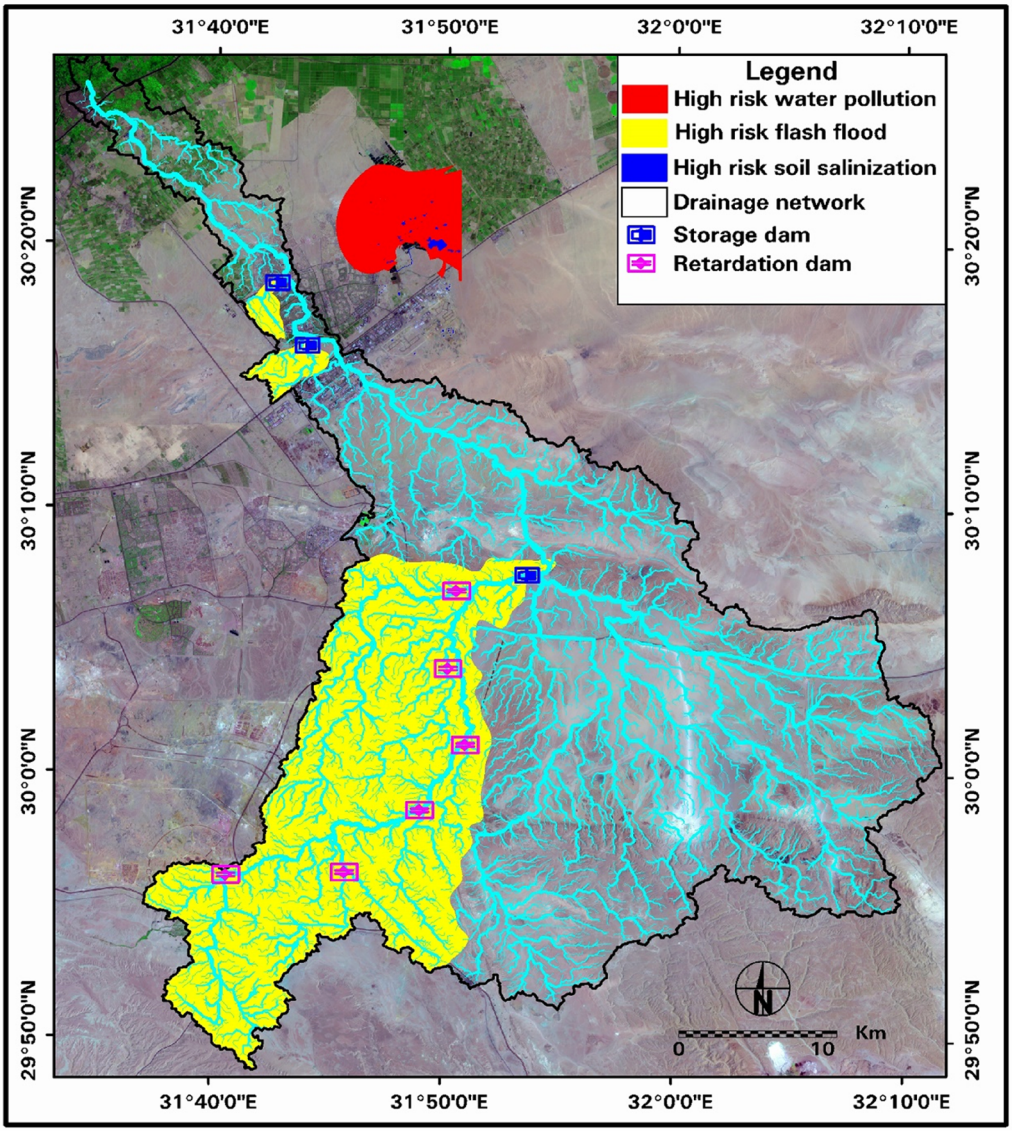

Fig. 17 The final geo-hazards risk map from the 10th RIR, including risk categories and distribution of controlling system (Storage and retardation dams) to mitigate the risk of flooding

The flood hazard map for the Wadi Gafra basin shows that sub-basins 1, 4, and 5 are at a high rank of flooding risk; sub-basins 2, 7, and 8 are at a moderate rank; and sub-basins 3, 9, and 10 are at a low rank.

The 10th RIR's integrated geo-hazards map shows that the high flash flood rank sub-basins are geospatially distributed in the southern parts of W. Gafra. Furthermore, the high groundwater-pollution zone is visible as geospatially distributed distinct areas, particularly in the northern zone of the 10th RIR and/or close to the oxidation ponds.

In summary, the study's findings reveal the impacts of flash floods on industrial facilities and the urban neighborhood in the 10th RIR and recommend mitigating actions. Based on the results of the current research, mitigation strategies should place an emphasis on low-cost hydraulic infrastructures, such as storage and retardation dams, in order to reduce the risk of flood damage and utilize the water for local consumption, which will help ensure the long-term sustainability of the 10th RIR. The results also revealed that the primary contributors to groundwater pollution in the 10th RIR were the leakage from nearby oxidation ponds and the consequences of returned flow irrigation wastewater. Groundwater can be prevented from contamination by lining oxidation pond bottoms with impervious

material like clay layer and purifying irrigation wastewater before practice as well.

The industrial wastewater from the 10th RIR is being illegally used in irrigation practices by surrounding farms. Future studies are needed to better understand how using industrial effluent for irrigation influences crops and those who eat them, especially regarding whether the crop products are healthy for human consumption. Such evidence is required if decision-makers and industrial owners are to be convinced to reduce and control environmental pollution. National and local efforts are required to change the situation. Legislation is required to enforce safety rules and prohibit dangerous chemicals, and pollutants in industrial discharges into groundwater.

Supplementary Information

The online version contains supplementary material available at https://doi.org/10.1186/s40068-023-00306-7.

Additional file 1: Figure S1. Field photographs showing the different types of environmental hazards prevailing the 10th RIR, where (A) Showing land deterioration caused by industrial waste dumping, (B) showing the feature of algae growth in wastewater reservoir, (C) showing surface industrial drain receiving piped wastewater discharge, and (D) showing a large surface reservoir containing mixed industrial wastewater inflow.

Author contributions

AE: Data analysis and interpretation of results and drafting, reviewing and submitting the original manuscript. MO: Data integration and GIS modeling and sharing the first draft of manuscript. DR: Interpreting field data, and reviewing the first draft. NF: Field data collection, analysis and interpretation of results and sharing the first draft.

Funding

The authors declare that no funds, grants, or other support were received during the preparation of this manuscript.

Availability of data and materials

All data generated or analyzed during this study are included in this published article.

Declarations

Ethics approval and consent to participate

Not applicable.

Consent for publication

Not applicable.

Competing interests

The authors have no relevant financial or non-financial interests to disclose.

Received: 3 May 2023 Accepted: 10 June 2023
Published online: 23 June 2023

References

Abu El Ela AI (2008) Environmental impact of the oxidation ponds of the industrial area of 10th of Ramadan city, Egypt. MSc Thesis, Faculty of Science, Mansoura University, Egypt

APHA (1971) Standard methods for the examination of water and wastewater. American Public Health Association, Washington D.C., 13th edn, p 874

Arnous MO (2004) Geo-environmental assessment of Cairo-Ismailia Road area, Egypt, using Remote Sensing and Geographic Information system (GIS). PhD Thesis, Geology Dept., Fac. of Science, Suez Canal Univ., Ismailia, p 283

Arnous MO (2011) Integrated remote sensing and GIS techniques for landslide hazard zonation: a case study Wadi Watier area, South Sinai, Egypt. J Coast Conserv 15(4):477–497. https://doi.org/10.1007/s11852-010-0137-9

Arnous MO (2016) Groundwater potentiality mapping of hard-rock terrain in arid regions using geospatial modelling: example from Wadi Feiran basin, South Sinai, Egypt. Hydrogeol J 24(6):1375–1392. https://doi.org/10.1007/s10040-016-1417-8

Arnous MO, El-Rayes AE (2013) An integrated GIS and hydrochemical approach to assess groundwater contamination in West Ismailia area, Egypt. Arab J Geosci 6(8):2829–2842. https://doi.org/10.1007/s12517-012-0555-0

Arnous MO, Green DR (2015) Monitoring and assessing waterlogged and salt-affected areas in the Eastern Nile Delta region, Egypt, using remotely sensed multi-temporal data and GIS. J Coast Conserv 19(3):369–391. https://doi.org/10.1007/s11852-015-0397-5

Arnous MO, Omar AE (2018) Hydrometeorological hazards assessment of some basin in Southwestern Sinai area, Egypt. J Coast Conserv 22(4):721–743. https://doi.org/10.1007/s11852-018-0604-2

Arnous MO, Aboulela HA, Green DR (2011) Geo-environmental hazards assessment of the north western Gulf of Suez, Egypt. J Coast Conserv 15(1):37–50. https://doi.org/10.1007/s11852-010-0118-z

Arnous MO, El-Rayes AE, Green DR (2015) Hydrosalinity and environmental land degradation assessment of the East Nile Delta region, Egypt. J Coast Conserv 19(4):491–513. https://doi.org/10.1007/s11852-015-0402-z

Arnous MO, El-Rayes AE, Helmy AM (2017) Land-use/land-cover change: a key to understanding land degradation and relating environmental impacts in Northwestern Sinai, Egypt. Environ Earth Sci 76(7):26. https://doi.org/10.1007/s12665-017-6571-3

Arnous MO, El-Rayes AE, Geriesh MH, Ghodeif KO, Al-Oshari F (2020) Groundwater potentiality mapping of tertiary volcanic aquifer in IBB basin, Yemen by using remote sensing and GIS tools. J Coast Conserv 24:27. https://doi.org/10.1007/s11852-020-00744-w

Attwa M, Gemail K, Eleraki M, Zamzam S (2013) Assessment of oxidation ponds impact using DC resistivity method in Tenth of Ramadan city, Egypt. The 20th International Geophysical Congress and Exhibition of Turkey, 25–27 November 2013, Antalya

Bell FG, Culshaw MG (1998) Some geohazards caused by soil mineralogy, chemistry and microfabric: a review. Geol Soc London Eng Geol Spl Publ 15:427–441

Chavez PS Jr (1996) Image-based atmospheric corrections-revisited and improved. Photogramm Eng Remote Sens 62:1025–1035

Chen Y-L, Shen S-L, Zhou A (2022) Assessment of red tide risk by integrating CRITIC weight method, TOPSIS-ASSETS method, and Monte Carlo simulation. Environ Pollut 314:120254. https://doi.org/10.1016/j.envpol.2022.120254

Chintalapudi P, Pujari P, Khadse G, et al (2017) Groundwater quality assessment in emerging industrial cluster of alluvial aquifer near Jaipur, India. Environ Earth Sci 76:8

Cigna F, Jordan H, Bateson L, McCormack H, Roberts C (2015) Natural and Anthropogenic Geohazards in Greater London Observed from Geological and ERS-1/2 and ENVISAT Persistent Scatterers Ground Motion Data: results from the EC FP7-SPACE PanGeo Project. Pure Appl Geophys 172(1):2965–2995

Climate-Data.org. (2013) Climate: 10th of Ramadan City-Climate graph, Temperature graph, Climate table. Retrieved 18 October

Dobrescu CF, Calarasu EA, Craifaleanu IG (2017) Ground settlement in urban structures exposed to geoenvironmental and anthropic hazards: a case study for Galati. Proc Eng 190:611–618

Elbeih SF, Madani AA, Hagage M (2021) Groundwater deterioration in Akhmim District, Upper Egypt: a remote sensing and GIS investigation approach. Egypt J Remote Sens Space Sci 24(3 Part 2):919–932

El-Dairy MD (1980) Hydrogeological studies on the eastern part of the Nile Delta using isotope techniques. MSc Thesis, University of Azhar, Egypt

Elewa HH, Shohaib RE, Qaddah AA, Nousir AM (2013) Determining groundwater protection zones for the Quaternary aquifer of northeastern Nile Delta using GIS-based vulnerability mapping. Environ Earth Sci 68(2):313–331
Elnemr A, Gad MI, Hussein EE (2015) Numerical simulation of groundwater flow and contaminant transport in the Quaternary aquifer in 10th of Ramadan city area, East Delta, Egypt. In: 8th international engineering conference. Faculty of Engineering, Mansoura University, Mansoura-Sharm El-Sheikh 17–22 Nov 2015 pp 202–222
El-Fayoumy IF (1968) Geology of groundwater supplies in the Eastern region of the Nile Delta and its extension in the North Sinai. PhD Thesis, Cairo University, Egypt
El-Shazly E, Abdel Hady M, El-Shazly MM, El-Ghawaby M, El-Khassas I, Salman A, Morsy M (1975) Geological and groundwater potential studies of Ismailia master plan study area. Remote Sensing Res. and Tech., Cairo, Egypt, pp 1–24
El-Rayes AE (2010) Hydrogeochemical prospecting of sulphide minerals in South Sinai, 1st edn. Lambert Academic Publishing, Germany
El-Rayes AE, Arnous MO, Aziz AM (2017) Morphotectonic controls of groundwater flow regime and relating environmental impacts in Northwest Sinai, Egypt. Arab J Geosci 10:401. https://doi.org/10.1007/s12517-017-3188-5
EL-Rayes AE, Arnous MO, Aboulela HA (2015) Hydrogeochemical and seismological exploration for geothermal resources in South Sinai, Egypt utilizing GIS and remote sensing. Arab J Geosci 8(8):5631–5647. https://doi.org/10.1007/s12517-014-1667-5
El-Sayed MH, El-Aassar AM, El-Fadl MMA, El-Gawad AMA (2012) Hydro-geochemistry and pollution problems in 10th of Ramadan City, East El-Delta, Egypt. J Appl Sci Res 8(4):1959–1972
Embaby AA, El Haddad IM (2007) Environmental impact of wastewater on soil and groundwater at the Tenth of Ramadan City area, Egypt. Mansoura J Geol Geophys 34(2):25–56
Farnham MW, Stephenson KK, and Fahey JW (2000) The capacity of broccoli to induce a mammalian chemoprotective enzyme varies among inbred lines. J Am Soc Hort Sci 125:482–488
Gad MI (1995) Hydrogeological studies for groundwater reservoirs, east of the Tenth of Ramadan City and vicinities. MSc Thesis, Ain Shams University, p 187
Gad M, El-Kammar MM, Ismail HMG (2015) Vulnerability assessment of the Quaternary aquifer of Wadi El-Tumilat, East Delta, using different overlay and index methods. Asian Rev Environ Earth Sci 2(1):9–22
Geriesh MH, Balke KD, El-Rayes AE (2008) Problems of drinking water treatment along Ismailia Canal Province. Egypt Int J Zhejiang Univ Sci B 9(3):232–242. https://doi.org/10.1631/jzus.B0710634,Springer
Ghodeif KO, Arnous MO, Geriesh MH (2013) Define a protected buffer zone for Ismailia Canal, Egypt using Geographic Information Systems. Arab J Geosci 6(1):43–53. https://doi.org/10.1007/s12517-011-0326-3
Gouda NF (2019) Assessment of some geohazards on 10th Ramadan area Egypt, using remote sensing and GIS technologies. MSc Thesis, Suez Canal Univ., Fac. of Sci., Geol. Dept., Ismailia, Egypt, p 150
Hadian MS, Azzy FN, Sophian, RI (2016) Geohazard and geological condition overview of Sekeloa-Bojongkoneng, Bandung, West Java-Indonesia. AIP Conf Proc 1730 (1) https://doi.org/10.1063/1.4947391
Hadley R and Schumm S (1961) Sediment sources and drainage basin characteristics in upper Cheyenne River basin. US Geological Survey Water-Supply Paper 153-B, Washington DC
Hefny K, Farid MS, Morsi A, Khater AR., El-Ridi MR, Khalil ZB, Atwia A, Attia D (1980) Groundwater studies for the tenth of Ramadan City. Unpublished internal report, Research Institute for Groundwater, Ministry of Public works and Water Researches, El Kanater, Cairo, Egypt, p 54
Horton RF (1932) Drainage basin characteristics. Trans Geophys Union 13:350–361
Horton RE (1945) Erosional development of streams and their drainage basins, hydrophysical approach to quantitative morphology. Geol Soc Am Bull 56:275–370
Hussein EE, Fouad M, Gad MI (2019) Prediction of the pollutant's movements from the polluted industrial zone in 10th of Ramadan city to the Quaternary aquifer. Appl Water Sci 9:20. https://doi.org/10.1007/s13201-019-0897-9
Hussien R, Hagagg K, El-Aassar AM (2017) Coupling HYDRUS and MODFLOW for studying environmental impact of wastewater ponds in tenth of Ramadan City, Egypt. Int J Eng Sci 6(10):41–54. https://doi.org/10.9790/1813-0610024154
Ibrahim SA, Eleraki M, Attwa MA (2005) Geoelectical resistivity, hydrogeology and hydrogeochemistry of unconsolidated aquifer at central southern part of the East Nile Delta, Egypt. J Petrol Mining Eng (JPME) 8:11–39
Ismael AMA (2007) Application of remote sensing, GIS, and groundwater flow modeling in evaluating groundwater resources: two case studies-East Nile Delta, Egypt and Gold Valley, California. PhD Thesis, University of Texas at El Paso, USA, ProQuest, 2007. ISBN: 0549355057-9780549355052, p 402
Jensen JR (2004) Introductory digital image processing: remote sensing perspective, 3rd edn. Prentice Hall, Upper Saddle River, NJ, p 544
Khalaf S, Gad M (2015) Modeling of contaminant transport in 10th of Ramadan City Area, East Delta, Egypt. Int J Water Resour Environ Eng 7(10):139–152. https://doi.org/10.5897/IJWREE2014.0616
Kotb M (2019) Climate change is a tangible reality on the ground. https://www.agri2day.com/2019/03/22 (in Arabic)
Krishnamurthy J, Kumar VN, Jayaraman V, Manivel M (1996) An approach to demarcate ground water potential zones through remote sensing and a Geographic Information System. Int J Remote Sens 17(10):1867–1884. https://doi.org/10.1080/01431169608948744
Kumar R, Kumar S, Lohani AK, Nema RK, Singh RD (2000) Evaluation of geomorphological characteristics of a catchment using GIS. GIS India, 9(3):13–17
Lin S-S, Shen S-L, Zhou A, Xu Y-S (2020) Approach based on TOPSIS and Monte Carlo simulation methods to evaluate lake eutrophication levels. Water Res 187:116437. https://doi.org/10.1016/j.watres.2020.116437
Lin S-S, Shen S-L, Zhang N et al (2022) An extended TODIM-based model for evaluating risks of excavation system. Acta Geotech 17:1053–1069. https://doi.org/10.1007/s11440-021-01294-7
Lyu H-M, Shen JS, Arulrajah A (2018) Assessment of geohazards and preventative countermeasures using AHP incorporated with GIS in Lanzhou, China. Sustainability 10(2):304. https://doi.org/10.3390/su10020304
Lyu H-M, Shen S-L, Zhou A, Yang J (2019) Risk assessment of mega-city infrastructures related to land subsidence using improved trapezoidal FAHP. Sci Total Environ 717:135310. https://doi.org/10.1016/j.scitotenv.2019.135310
Lobo-Ferreira JP, Oliveira MM (1997) DRASTIC groundwater vulnerability mapping of Portugal. In Groundwater: an endangered resource. Proceedings of Theme C of the 27th Congress of the International Association for Hydraulic Research. San Francisco, USA, August 1997, pp 132–137
Maidment DR (2002) Arc Hydro: GIS for water resources. ESRI Press, California, USA, p 206
Mejfa-Navarro M, Wohl EE, Oaks SD (1994) Geological hazards, vulnerability, and risk assessment using GIS: model for Glenwood Springs, Colorado. Geomorphology 10:331–354
Miller VC (1953) A quantitative geomorphic study of drainage basin characteristics in the Clinch Mountain Area Virginia and Tennessee. DTIC Document
Mondal T, Gupta S (2015) Evaluation of morphometric parameters of drainage networks derived from topographic map and digital elevation model using remote sensing and GIS. Int J Geomat Geosci 5(4):655–664
Moubarak AH, Arnous MO, El-Rayes AE (2021) Integrated geoenvironmental and geotechnical risk assessment of East Port Said Region, Egypt for Regional Development. Geotech Geol Eng 39(2):1497–1520. https://doi.org/10.1007/s10706-020-01571-4
Naghibi SA, Pourghasemi HR, Pourtaghi ZS, Rezaei A (2015) Groundwater Qanat potential mapping using frequency ratio and Shannon's Entropy Models in the Moghan Watershed, Iran. Earth Sci Inform 8(1):171–186
Omran A, Fahmida K, Schröder D, Arnous MO, El-Rayes AE, Hochschild V (2021) GIS-based rockfall hazard zones modeling along the coastal Gulf of Aqaba Region, Egypt. Earth Sci Inform 14(9):1–19. https://doi.org/10.1007/s12145-021-00580-y
Omran AF, Schroder D, El-Rayes AE, Geriesh MH (2011) Flood hazard assessment in Wadi Dahab, Egypt based on basin morphometry using GIS techniques. In: Car A, Griesebner G, Strobl J (eds) Geospatial crossroads @ GI-Forum '11. ©Herbert Wichmann Verlag, VDE VERLAG GMBH, Berlin/Offenbach. ISBN 978-3-87907-509-6.
Rai PK, Mohan K, Mishra S, Ahmed A, Mishra VN (2014) A GIS-based approach in drainage morphometric analysis of Kanhar River basin, India. Appl Water Sci 7:217–232. https://doi.org/10.1007/s13201-014-0238-y

Ramkumar Mu (2009) Geological hazards: causes, consequences and methods of containment. New India Publishing Agency, Pitam Pura, New Delhi, 110088, India, p 328
Ren T, Jiang R, Guo L, Zhang H, Yang S (1989) A geochemical well water survey in arid and semiarid regions. J Geochem Explor 33:47–59
Sandler D, Schwab AK (2022) Hazard mitigation and preparedness: an introductory text for emergency management and planning professionals, 3rd edn. Routledge Publication, New York
Saraf A, Choudhury P (1998) Integrated remote sensing and GIS for groundwater exploration and identification of artificial recharge sites. Int J Remote Sens 19(10):1825–1841
Said R (1990) The geology of Egypt. Elsevier, Amsterdam
Said R (1981) The geological evolution of the River Nile. Springer, New York
Schumm SA (1956) Evolution of drainage system and slopes in badlands at Perth Amboy. N Jersey Geophys Soc Am Bull 67:597–646
Sherif MM (1999) The Nile Delta aquifer in Egypt. In: Bear J, Cheng A, Sorek S, Ouazar D, Herrera A (eds) Seawater intrusion in coastal aquifers: concepts, methods and practices. Book series: theory and application of transport in Porous Media, vol 14. Kluwer Academic Publishers, Netherlands, pp 559–590
Shvartsev SL, Udodov PA, Rasskazove NM (1975) Some features of the migration of microcomponents in natural waters of the supergene zone. J Geochem Explor 4:433–439
Sims D (2010) Understanding Cairo: the logic of a city out of control. The American University in Cairo Press
Srinivasa Rao Y, Jugran D (2003) Delineation of groundwater potential zones and zones of groundwater quality suitable for domestic purposes using remote sensing and GIS. Hydrol Sci J 48(5):821–833
Strahler AN (1952) Dynamic basis of geomorphology. Geol Soc Am Bull 63(9):923–938
Strahler A (1958) Dimentional analysis applied to fluvially eroded landforms. GSA Bulletin 69 (3):279–300. https://doi.org/10.1130/0016-7606(1958)69[279:DAATFE]2.0.CO;2
Strahler AN (1964) Quantitative geomorphology of drainage basins is channel networks. In: Hill McGraw (ed) Hand book of applied hydrology, Vent Te Chow. Book Company, New York, pp 39–79
Sun Q, Zhang J, Zhang Q, Zhao X (2017) Analysis and prevention of geo-environmental hazards with high-intensive coal mining: a case study in China's Western eco-environment Frangible Area. Energies 10:786. https://doi.org/10.3390/en10060786
Suk HJ and Lee K-K. (1999) Characterization of a ground water hydrochemical system through multivariate analysis: clustering into ground water zones. Ground Water 37:358–366
Swanson SK, Bahr JM, Schwar MT, Potter KW (2001) Two-way cluster analysis of geochemical data to constrain spring source waters. Chem Geol 179(1–4):73–91. https://doi.org/10.1016/S0009-2541(01)00316-3
Taha AA, El-Mahmoudi AS, El-Haddad IM (2004) Pollution sources and related environmental impacts in the new communities southeast Nile Delta, Egypt. Emirates J Eng Res 9(1):35–49
Topographic maps of Eastern Nile Dalta region (1987) Egyptian Military Survey Department, Cairo, Egypt
WHO (1996) Guidelines for drinking water quality. Health criteria and other supporting information, 2nd edn. World Health Organization, Geneva
Yan T, Shen S-L, Zhou A (2022) Indices and models of surface water quality assessment: review and perspectives. Environ Pollut 308:119611. https://doi.org/10.1016/j.envpol.2022.119611
Zhang XU, Zhou T, Zheng J (2009) DEM-based spatial discretization and parameter database design for distributed hydrological model. Proc. SPIE 7498, MIPPR 2009: Remote Sensing and GIS Data Processing and Other Applications, 749831 (October 30, 2009). https://doi.org/10.1117/12.832487

Publisher's Note